

*FE Simulations of Mounting of an
Anisotropic Work Piece Material to
Reduce the Effects of Vibration*

Punith Prakash

Sudarshan Girigimmalayanapalya Shivanna

CODEN:LUTMDN/(TMMV-5322)/1-71/2021



LTH
FACULTY OF
ENGINEERING

MASTER THESIS
DIVISION OF PRODUCTION AND MATERIALS
ENGINEERING
LUND UNIVERSITY

Supervisor: Aylin Ahadi
Co-supervisor: Solveig Melin
Examiner: Kristina Nilsson

Authors:
Prakash
Sudarshan Girigimallayanapalya Shivanna

Avdelningen för Industriell Produktion
Lunds Tekniska Högskola
Lunds universitet
Box 118
221 00 Lund
Sverige

Division of Production and Materials Engineering
LTH, School of Engineering
Lund University
Box 118
SE-221 00 Lund
Sweden

Foreword

This degree project has been carried out as a cooperation between the Division of Mechanics and division of Production and Materials Engineering at Lund University. It was supervised by Professor Aylin Ahadi at the Division of mechanics, co-supervised by Professor Solveig Melin at the Division of mechanics, and examined by Professor Kristina Nilsson at the Division of mechanics.

We first and foremost wish to express our gratitudes to Aylin and Solveig for assisting us in various ways during this project and for sharing their knowledge and thank you for your patience, as well as we thank Kristina for taking on the role as our examiner.

We would also like to thank all of the faculty members in the division of Production and Materials Engineering at Lund University for their outstanding efforts in shaping our academics and for everything they have done over the last two years. Thank you for making our time in LTH memorable.

Lund 2021-06-02

Punith Prakash and Sudarshan Girigimallayanapalya Shivanna

Abstract

Optical cavities should be designed to be insensitive to vibration in all directions. The study of the behavior of the material used to develop an optical cavity is vital for the cavity to be insensitive in all orders. In this project, we are using Abaqus to generate a FE model of an optical cavity and its mountings via support points in order to investigate the effects of vibration in different directions during machining. In any machining operation, mounting the workpiece is critical, and it is one of the most critical factors in reducing vibration, by varying mounting orientations.

The work begins with the recreation and development of a FE model in Abaqus with appropriate boundary conditions as in the reference paper [1]. To achieve the desired results, various load and boundary conditions were simulated. Material properties were varied for the same model with obtained boundary and load conditions, and differences in deformation and stress patterns are presented in this paper.

The optimal mounting position was chosen to investigate the anisotropy material behavior for different orientations by varying the stacking directions. The effects and sensitivity of vibrations due to external loading on optical cavities for different anisotropy material orientations were investigated. Finally, modal analysis was performed for the selected model properties and mounting position to investigate the system's natural frequencies and behavior.

Keywords : Optical cavity, Anisotropy material, FE simulation, Modal analysis.

Contents

1	Introduction	10
1.1	Background	10
1.2	Aim and Purpose	11
1.3	Disposition of Report	11
2	Theory	12
2.1	General Process of Machining	12
2.2	Vibrations	13
2.2.1	Mathematical Model - Vibration	13
2.3	Anisotropic Material	14
2.4	Modal Analysis	16
2.4.1	Modal Testing	17
2.4.2	Mathematical Model – Modal Analysis	17
2.4.3	Single Degree of Freedom	18
2.5	Finite Element Analysis	19
3	Methodology	22
3.1	CAD Geometry	24
3.2	Material Model	25
3.3	Step	25
3.4	Boundary and load conditions	26
3.5	Meshing of the model	27
4	Results	29
4.1	Simulation of cylindrical model	29
4.1.1	Cylindrical model with isotropic material properties	29
4.1.2	Cylindrical model with anisotropic material properties	32
4.2	Simulation of Rectangular model	39
4.2.1	Rectangular model with isotropic material properties	39
4.2.2	Rectangular model with anisotropic material properties	41
4.3	Modal analysis	47
4.3.1	Modal analysis of cylindrical model with isotropic material properties	47
4.3.2	Modal analysis of rectangular model with isotropic material properties	55
5	Discussion and Conclusions	64

List of Figures

1	<i>Cylindrical spacer cavity [1]</i>	10
2	<i>Two different simple vibratory systems [2]</i>	13
3	<i>Schematic representation of an anisotropic and isotropic two- dimensional material response upon the application of normal strains.[3]</i>	15
4	<i>One dimensional line element have trusses, beams and boundary elements [4]</i>	20
5	<i>Two-dimensional plane elements has plane stress, plane strain, axisymmetric, membrane and shell elements [4]</i>	20
6	<i>Three-dimensional volume elements has tetrahedral, hexahedral and brick elements [4]</i>	21
7	<i>Working procedure used to develop the FE model</i>	23
8	<i>Cylindrical spacer cavity model</i>	24
9	<i>Rectangular spacer cavity model</i>	24
10	<i>Step instance</i>	26
11	<i>Applied load and boundary conditions for cylindrical model</i>	27
12	<i>Applied load and boundary conditions for rectangular model</i>	27
13	<i>Meshed image of cylindrical model</i>	28
14	<i>Meshed image of rectangular model</i>	28
15	<i>Simulated deformation in X-direction under an 0.1 m/s² acceleration in Y-direction</i>	30
16	<i>Simulated deformation in Z-direction under an 0.1 m/s² acceleration in Y-direction</i>	30
17	<i>Von-Mises stress distribution under an 0.1 m/s² acceleration in Y-direction</i>	31
18	<i>Maximum principal stress distribution under an 0.1 m/s² acceleration in Y-direction</i>	31
19	<i>Simulated deformation in X-direction under an 0.1 m/s² acceleration in Y-direction</i>	32
20	<i>Simulated deformation in Z-direction under an 0.1 m/s² acceleration in Y-direction</i>	33
21	<i>Von-Mises stress distribution under an 0.1 m/s² acceleration in Y-direction</i>	33
22	<i>Maximum principal stress distribution under an 0.1 m/s² acceleration in Y-direction</i>	34
23	<i>Simulated deformation in X-direction under an 0.1 m/s² acceleration in Y-direction with 90 degrees additional rotation of orientation</i>	35
24	<i>Simulated deformation in Z-direction under an 0.1 m/s² acceleration in Y-direction with 90 degrees additional rotation of orientation</i>	35
25	<i>Von-Mises stress distribution under an 0.1 m/s² acceleration in Y-direction with 90 degrees additional rotation of orientation</i>	36
26	<i>Maximum principal stress distribution under an 0.1 m/s² acceleration in Y-direction with 90 degrees additional rotation of orientation</i>	36
27	<i>Simulated deformation in X-direction under an 0.1 m/s² acceleration in Y-direction with 270 degrees additional rotation of orientation</i>	37

28	<i>Simulated deformation in Z-direction under an 0.1 m/s² acceleration in Y-direction with 270 degrees additional rotation of orientation . . .</i>	37
29	<i>Von-Mises stress distribution under an 0.1 m/s² acceleration in Y-direction with 270 degrees additional rotation of orientation</i>	38
30	<i>Maximum principal stress distribution under an 0.1 m/s² acceleration in Y-direction with 270 degrees additional rotation of orientation . .</i>	38
31	<i>Simulated deformation in X-direction under an 0.1 m/s² acceleration in Y-direction</i>	39
32	<i>Simulated deformation in Z-direction under an 0.1 m/s² acceleration in Y-direction</i>	40
33	<i>Von-Mises stress distribution under an 0.1 m/s² acceleration in Y-direction</i>	40
34	<i>Maximum principal stress distribution under an 0.1 m/s² acceleration in Y-direction</i>	40
35	<i>Simulated deformation in X-direction under an 0.1 m/s² acceleration in Y-direction</i>	41
36	<i>Simulated deformation in Z-direction under an 0.1 m/s² acceleration in Y-direction</i>	41
37	<i>Von-Mises stress distribution under an 0.1 m/s² acceleration in Y-direction</i>	42
38	<i>Maximum principal stress distribution under an 0.1 m/s² acceleration in Y-direction</i>	42
39	<i>Simulated deformation in X-direction under an 0.1 m/s² acceleration in Y-direction with 90 degrees additional rotation of orientation . . .</i>	43
40	<i>Simulated deformation in Z-direction under an 0.1 m/s² acceleration in Y-direction with 90 degrees additional rotation of orientation . . .</i>	43
41	<i>Von-Mises stress distribution under an 0.1 m/s² acceleration in Y-direction with 90 degrees additional rotation of orientation</i>	44
42	<i>Maximum principal stress distribution under an 0.1 m/s² acceleration in Y-direction with 90 degrees additional rotation of orientation . . .</i>	44
43	<i>Simulated deformation in X-direction under an 0.1 m/s² acceleration in Y-direction with 270 degrees additional rotation of orientation . .</i>	45
44	<i>Simulated deformation in Z-direction under an 0.1 m/s² acceleration in Y-direction with 270 degrees additional rotation of orientation . .</i>	45
45	<i>Von-Mises stress distribution under an 0.1 m/s² acceleration in Y-direction with 270 degrees additional rotation of orientation</i>	46
46	<i>Maximum principal stress distribution under an 0.1 m/s² acceleration in Y-direction with 270 degrees additional rotation of orientation . .</i>	46
47	<i>First 10 mode Natural frequencies (fn) of the isotropic cylindrical model</i>	47
48	<i>Initial 10 modes of frequencies of isotropic cylindrical model</i>	48
49	<i>First 10 mode Natural frequencies (fn) of the anisotropic cylindrical model</i>	49
50	<i>Initial 10 modes of frequencies of anisotropic cylindrical model</i>	50
51	<i>First 10 mode Natural frequencies(fn) of the anisotropic cylindrical model</i>	51
52	<i>Initial 10 modes of frequencies of anisotropic cylindrical model</i>	52

53	<i>First 10 mode Natural frequencies(fn) of the anisotropic cylindrical model</i>	53
54	<i>Initial 10 modes of frequencies of anisotropic cylindrical model</i>	54
55	<i>First 10 mode Natural frequencies(fn) of the isotropic rectangular model</i>	55
56	<i>Initial 10 modes of frequencies of isotropic rectangular model</i>	56
57	<i>First 10 mode Natural frequencies(fn) of the isotropic rectangular model</i>	57
58	<i>Initial 10 modes of frequencies of isotropic rectangular model</i>	58
59	<i>First 10 mode Natural frequencies(fn) of the isotropic rectangular model</i>	59
60	<i>Initial 10 modes of frequencies of isotropic rectangular model</i>	60
61	<i>First 10 mode Natural frequencies(fn) of the isotropic rectangular model</i>	61
62	<i>Initial 10 modes of frequencies of isotropic rectangular model</i>	62
63	<i>Mode number vs frequency for cylindrical model</i>	63
64	<i>Mode number vs frequency for rectangular model</i>	63

Nomenclature

Abbreviations and Acronyms

Abbreviation / Symbols	Meaning
FEM	Finite Element Modeling
FEA	Finite Element Analysis
DOF	Degree-Of-Freedom
SDOF	Single-Degree-Of-Freedom
MDOF	Multiple-Degree-Of-Freedom
FRF	Frequency Response Function
CFD	Computational fluid dynamics
CAE	Computer-aided engineering
m	Mass
$f(t)$	Externally applied force
$mx(t)$	Inertial force
$cx(t)$	Damping internal force
$kx(t)$	Restoring force
$x(t)$	Position of mass
σ_{ij}	Stress Component
C_{ijkl}	Elastic constant or Moduli
ε_{kl}	Strain component
$Z(s)$	Dynamic stiffness
$H(i\omega)$	Frequency Response Function

1 Introduction

This research includes a FE simulation in Abaqus software to investigate the differences in vibration effects and behavior between an anisotropic and isotropic optical cavities using appropriate load and boundary conditions, as well as a modal analysis is performed in the end. The history of the subject and the work's goal and intent are all covered in this chapter.

1.1 Background

Ultra-stable laser light is used in a wide range of applications, including optical frequency standards, relativity experiments, the generation of low-phase-noise microwave signals, and the transmission of optically stable frequencies over fiber networks as well as gravitational wave detection[5]. Furthermore, they are critical in high-resolution spectroscopy, fundamental physics experiments, and interferometric measurements such as future space flights, including the laser interferometer[1]. These new approaches to the design of Fabry-Perot reference cavities, which are used to stabilize lasers, have been sparked by these research topics, especially cold atoms, and single-ion optical frequency standards[5].

The dick effect limits the clock frequency stability of optical frequency standards with neutral atoms due to the frequency noise of state-of-the-art ultra-stable clock lasers[6]. Because of this restriction, the best recorded Allan deviations are more than one order of magnitude greater than the clocks' ultimate quantum limit[7]. Reducing the spectral density of the laser's frequency noise in the low frequency range to achieve ultimate stability close to the quantum projection limit[5].

The effect of residual vibration must be minimized to reduce the frequency noise of stabilized laser cavities[8]. While vibration isolation systems can reduce noise, most compact commercial systems are insufficient to achieve a sub-hertz laser line width[9]. By carefully designing the geometry of the cavity and its mounting, one way to increase the spectral efficiency of the stabilized laser is to reduce vibration sensitivity[10].

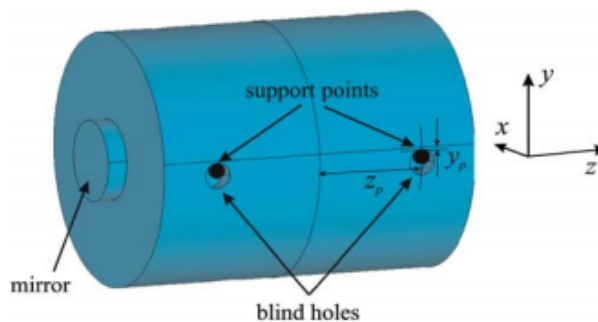


Figure 1: *Cylindrical spacer cavity [1]*

The figure 1 shows the cylindrical cavity mounting, which will be recreated in this paper. The initial focus here is to reduce the vibration of the spacer cavity by optimizing the mounting positions. Later for the obtained mounting position, the vibration sensitivity of different material properties will be analyzed.

1.2 Aim and Purpose

This master's project aims to recreate an FE model of the workpiece in Abaqus software, followed by appropriate boundary conditions to investigate the different mounting positions and responses to different material properties. This project aims to study the best possible stress-free mounting orientation by simulation, which helps to reduce the vibration of the workpiece. Then the modal analysis is performed for the least vibrating mounting position to study its range of natural frequencies. By Completing all the simulations, sensitivity to vibration will be investigated and analyzed, which were induced due to the external loading for different orientations of the anisotropic workpiece.

1.3 Disposition of Report

The report begins with details about the thesis's context, goal, intent, and limitations. Then, it briefly outlines the science behind machining and vibrations, including the fundamentals of anisotropic materials and the concept of modal analysis, and its significance using the Finite element method. The methodology is then presented, which includes the procedure used in the thesis, the software used, the boundary conditions and loads used in the simulations, and post- processing of the data. Following the methodology, the results are described in tables and figures in the following section, which contains relevant details from the simulations with brief comments to the corresponding figures. In the discussion portion, the majority of the findings are anatomized with explanations. In the conclusion section, the most significant observations are summarized and represented.

2 Theory

This section is organized as follows: an overview of current machining process understanding with mounting positions, vibrations, anisotropic material descriptions, modal analysis, and finally finite element analysis.

2.1 General Process of Machining

Machining is a material removal process from a workpiece in the form of powder, chips, and parts at a regulated rate and condition in order to give the workpiece the desired shape and size by applying external force or load[11]. Material removal for workpieces is done in all machining processes by applying load or forces with or without cutting equipment[12]. So, regardless of the machining method, the application of external pressure or load, whether conventional or non-conventional, is needed[13]. The force or load is applied in conventional machining by various cutting tools that come into contact with the workpiece[14]. The load application approach differs from traditional methods such as different cutting tools and non-conventional techniques such as chemical and other energy sources in non-conventional methods[15].

The applied loads, forces, friction, and other energy sources for the machining process are transformed into another form in all machining processes[16]. Heat, vibration, and stress will be produced in the workpieces due to the converted load or energy applied. These outcomes for the process cannot be removed, but they can be reduced or regulated[17]. Heat, vibration, and stress will trigger issues during machining and affect the machining process final product[18]. The analysis of these outcomes during machines is more important to minimize and improve the machining process's performance[19].

In any machining method, mounting is one of the most basic functions. During machining, mounting limits the movement of the material or workpiece to a single location. During the machining process, all workpieces should be secured to some mounting system to exploit the forces applied by the cutting tools fully. The importance of the mounting process and its mechanisms in precision machining at the micro and nanoscale and the machining of small workpieces are of greater importance[20].

During machining, vibration is caused by the relative motion between the workpiece and the cutting tool. This vibration influences the result of the machining process. This vibration can be minimized by adding a damping effect or using proper mounting techniques[21]. When it comes to machining anisotropic materials, anisotropy is a big issue. These materials are difficult to machine due to their properties, which vary depending on the direction in which they are processed. As a result, it is more necessary to study anisotropic materials before machining[22].

2.2 Vibrations

Vibration is a self-repeating motion. This pattern may or may not continue. It's also not necessary for the replication to be a literal duplicate. In a statistical scene, specific vibrations can repeat themselves[23]. The presence of inertial and elastic components like mass and spring are not the vital elements for vibration. Since vibration is described as the transfer of kinetic and potential energy, a vibratory device must provide a mechanism for storing both of these energies[24]. The former is often accomplished by a mass, while the latter is performed by a spring. A typical vibratory mechanism is shown in Figure 2 as a mass connected to a horizontal spring. The mass is in charge of kinetic energy, while the spring is in charge of potential energy. A pendulum may also represent a vibratory mechanism.

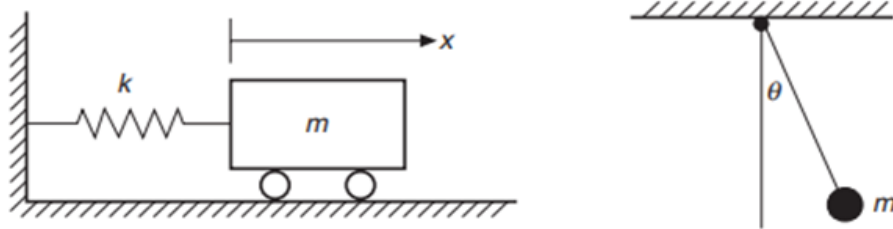


Figure 2: *Two different simple vibratory systems [2]*

There is no spring-like part for potential energy in this device. In reality, mass serves as a source of both kinetic and potential energy. This illustration refutes the belief that a vibratory machine must have both mass and stiffness components. Before analyzing a dynamic system's vibration, it is essential to know how many degrees of freedom the design has. The number of DOF in a vibratory system is defined as the smallest number of independent coordinates needed to fully determine the motion of all system components at any given time[2].

2.2.1 Mathematical Model - Vibration

Vibration issues can range from basic to complex. Except for those structures whose dynamics can be adequately represented by a finite number of partial differential equations, vibration theory seldom applies directly to an existing system[25]. This is because a theory is typically formulated for a simplified version of a particular problem based on a set of assumption. Not all these assumptions are quickly spelled out. Mathematical Modeling for the structure is the method of idealizing a particular structure until it can be analyzed.

The model created by the idealization process for an actual structure is not unique. The need to derive a basic, accurate, and easy-to-understand model is a challenge that can be faced by both experience and a deep understanding of dynamics[26].

The mathematical model for modal analysis is often discretized with a finite number of coordinates. A chosen spatial resolution is used to reflect continuous behavior, such as mode shapes. As a result, the model is often expressed as a collection of ordinary equations. These equations can be translated into algebraic equations using the Laplace or Fourier transform. This emphasizes the significance of material algebra in modal analysis[2].

2.3 Anisotropic Material

Anisotropy refers to properties of the substance or material in which those material properties vary with respect to the direction in or along with the measurement. Anisotropic materials are also called direction dependency materials. Isotropic on the other hand in which material properties are same irrespective of direction of measurement. Authors need to know the effect of anisotropy on the materials behavior under the application of load. mechanical response of anisotropic materials are preferred by the presence of one or more directions[27].

Machining of the anisotropic materials is difficult not only because of hardness and brittleness but also because of structural anisotropy of the materials[28]. For elastic materials, inversion of linear stress-strain relations is often theoretically feasible, allowing for immediate determination of the strain associated with characterization tests. For isotropic materials, this inversion is easy, but for anisotropic materials, the process can be extremely difficult[29]. The magnitude of the applied strain is significant in anisotropic material designs. Their material properties are highly dependent on the applied deformation, with highly nonlinear constitutive law behavior being typical[30][31]. Anisotropic material designs are appealing not only because of stiffness requirements but also because of volumetric behaviors. Near-zero Poisson's ratio values, in particular, have been found to favor nanoengineering applications[32].

The deformation mechanism is strongly affected by structural anisotropy. Because of this, load application on anisotropic materials is complex. An investigation of anisotropic materials is usually accompanied by a study of isotropic materials, which have mechanical responses that are independent of direction and therefore have a straightforward mathematical theory. The design of ideal wind morphing structures has been linked to the creation of highly anisotropic artificial materials. Furthermore, various mechanical engineering, such as ceramics and the automotive industry, require lightweight synthetic materials with direction-based static properties[33][34]. The figure 3 gives the brief view of the difference between the isotropic and anisotropic materials response due to the application of force along the different direction.

Elastic constants are parameters that express the relationship between stress and strain on materials in the stress range where they exhibit elastic behavior[35]. Elastic constants are fundamental properties that specify how a crystal reacts to a load applied from the outside. They include information on the chemical bonding as well as the solid's mechanical and structural stability[36]. The elastic constants that

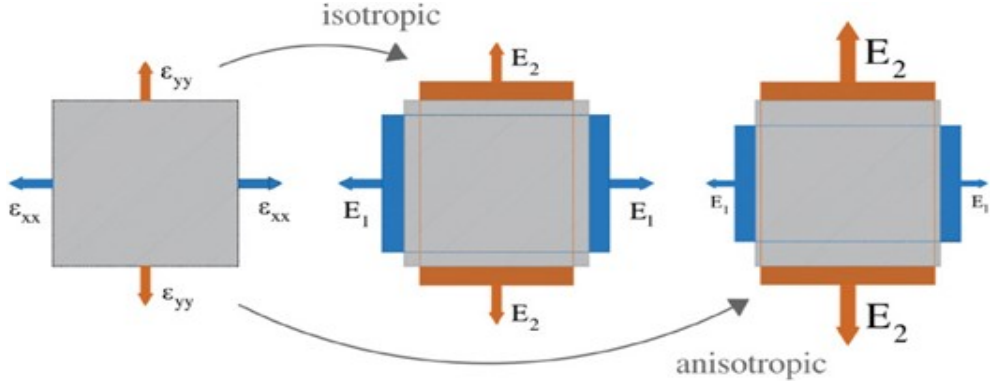


Figure 3: Schematic representation of an anisotropic and isotropic two-dimensional material response upon the application of normal strains.[3]

make up the stiffness matrix are not explicitly calculated in a material's laboratory. Laboratory experiments may be used to determine engineering constants such as Young's modulus, shear modulus, and Poisson's ratio. Stiffness matrix of the elastic constants and engineering constant does not have any direction connection. With the help of engineering constants and compliance matrix coefficient, equation 2 can be formed [37].

The elastic constant of the anisotropic material can be finding by different material depending on the type of material. With the help of hook's law elastic constants can be calculated, common anisotropic material with a linear elastic behavior can be expressed with stress-strain relationship as follow,

$$\sigma_{ij} = C_{ijkl}\varepsilon_{kl} \quad (1)$$

Where:

- σ_{ij} : stress component
- C_{ijkl} : elastic constant or moduli
- ε_{kl} : strain component

$$\begin{bmatrix} \sigma_1 = \sigma_{xx} \\ \sigma_2 = \sigma_{yy} \\ \sigma_3 = \sigma_{zz} \\ \sigma_4 = \sigma_{yz} \\ \sigma_5 = \sigma_{xz} \\ \sigma_6 = \sigma_{xy} \end{bmatrix} = \begin{bmatrix} C_{11} & C_{12} & C_{13} & C_{14} & C_{15} & C_{16} \\ C_{21} & C_{22} & C_{23} & C_{24} & C_{25} & C_{26} \\ C_{31} & C_{32} & C_{33} & C_{34} & C_{35} & C_{36} \\ C_{41} & C_{42} & C_{43} & C_{44} & C_{45} & C_{46} \\ C_{51} & C_{52} & C_{53} & C_{54} & C_{55} & C_{56} \\ C_{61} & C_{62} & C_{63} & C_{64} & C_{65} & C_{66} \end{bmatrix} \begin{bmatrix} \varepsilon_1 = \varepsilon_{xx} \\ \varepsilon_2 = \varepsilon_{yy} \\ \varepsilon_3 = \varepsilon_{zz} \\ \varepsilon_4 = \varepsilon_{yz} \\ \varepsilon_5 = \varepsilon_{xz} \\ \varepsilon_6 = \varepsilon_{xy} \end{bmatrix} \quad (2)$$

In the above matrix Equation 2 each stress components are depending on all strain components. With the help of numbering the stress and strain components, the equation anisotropic elasticity can be written in the matrix form as above. The 36 C_{ij} are material constants called as stiffness. The matrix is called as stiffness matrix. Form the principle of symmetric properties, the whole matrix is symmetrical and only 21 independent material constants will be obtaining in the case of anisotropic

material. Therefore, in the above matrix due to symmetry bottom half can be eliminated and the matrix can be simplified as below Equation 3,

$$\begin{bmatrix} \varepsilon_1 \\ \varepsilon_2 \\ \varepsilon_3 \\ \varepsilon_4 \\ \varepsilon_5 \\ \varepsilon_6 \end{bmatrix} = \begin{bmatrix} S_{11} & S_{12} & S_{13} & S_{14} & S_{15} & S_{16} \\ & S_{22} & S_{23} & S_{24} & S_{25} & S_{26} \\ & & S_{33} & S_{34} & S_{35} & S_{36} \\ & & & S_{44} & S_{45} & S_{46} \\ & & & & S_{55} & S_{56} \\ & & & & & S_{66} \end{bmatrix} \begin{bmatrix} \sigma_1 \\ \sigma_2 \\ \sigma_3 \\ \sigma_4 \\ \sigma_5 \\ \sigma_6 \end{bmatrix} \quad (3)$$

Due to a large number of elastic constants, completely anisotropic materials are challenging to model. Fortunately, many materials that aren't isotropic do have certain material symmetries that make the equations 2 and 3 above easier to understand[38].

2.4 Modal Analysis

One of the most critical methods in searching to determine, improve, and optimize the complex characteristics of engineering is modal analysis. The method of evaluating a system's inherent dynamics characteristics, such as natural frequencies, damping factors, and mode shapes, and using them to develop a mathematical model for its dynamic behavior is known as modal analysis [39]. Modal data is the information gathered as characteristics, and the developed mathematical model is known as the modal model of the system[40].

Frequency and orientation are used to decompose the dynamics of a structure physically. According to modal analysis, the vibration response of a linear time-invariant dynamic system can be expressed as a linear combination of a series of simple harmonic motions called natural modes of vibration[41]. A Fourier method of sine and cosine waves is used to describe a complicated waveform[42]. A dynamic system's natural modes of vibration are determined entirely by its physical properties such as mass, stiffness, damping, etc., and their spatial distributions. The natural frequency, the modal damping factors, and the characteristic displacement pattern, namely mode form, are all modal parameters for each mode[43].

Modes are intrinsic properties of an elastic structure that are determined by material properties (mass, damping, and stiffness), as well as the structure's boundary conditions change, the structure's modes change as well. When a mass is applied to a system, for example, it vibrates differently[44].

The form of the mode may be complex or straightforward. Each one is associated with a natural frequency. The degree to which each natural mode participates in the overall vibration is determined by the properties of the excitation sources as well as the system's mode shape[45].

Theoretical and experimental approaches are combined in modal analysis. Theoret-

ical modal analysis is based on a physical modal of a dynamic system that includes mass, stiffness, and sampling characteristics. These characteristics can be expressed as partial differential equations. The equation of wave of a constant vibratory string derived from its mass distribution and elasticity properties is an example[46]. The equation's solution yields the string's natural frequencies and mode forms, as well as its forced vibration responses. A more practical model, on the other hand, would typically include the mass, stiffness, and damping properties as spatial distributions, i.e., the mass, stiffness, and damping matrices. These matrices are used to solve a series of ordinary differential equations of motion. We can convert these equations into a standard edge value problem using the superposition principle of a linear dynamic system. Its solution provides the system's modal results[47].

Modern finite element analysis allows almost every linear dynamic structure to be discretized, significantly expanding the potential and range of theoretical modal analysis. On the other hand, significant developments in the experimental field of research, known as modal testing, have resulted from the rapid growth of data collection and processing capabilities over the last two decades[2].

2.4.1 Modal Testing

It is an experimental technique for determining a linear time-invariant vibratory system's modal model. The three steps of experimental modal analysis are test planning, frequency response measurements, and modal parameter recognition. Selection of a structure's type of support, type of excitation force, location of excitation, hardware to measure the force contains points of response to be measured; and identification of mechanisms that could contribute to incorrect measurement are all part of the test preparation process. A set of frequency response function data is collected and stored during the test, then analyzed to determine the evaluated structure's modal parameters[48].

2.4.2 Mathematical Model – Modal Analysis

Math is used in modal analysis to create theoretical models for complex system and analyse data in different formats. Since modal analysis includes both time domain and frequency domain analysis, the mathematics involved is extensive. It deals with both discretised and continuous dynamic processes[49]. Curve fitting, matrix manipulation, statistical analysis, parameter recognition, and other analytical and numerical studies were conducted. As a consequence, proper mathematical planning is needed.

In modal analysis, matrix theory is critical. This because modal analysis theory is focused on the study of a multi-degree-of-freedom dynamic structure, which is based primarily on matrix theory. The solution of linear equations, matrix inverse, and edge value problems are the most common matrix analyses.

In modal analysis, the Fourier transform is essential for signal processing. The quick

Fourier transform is widely regarded as a watershed moment in the advancement of modal analysis technology. Modal research would always be an empirical and scientific endeavor without it[44].

2.4.3 Single Degree of Freedom

In the Time domain, the following Equation 4 describes a single-degree-of-freedom mechanism, where the mass m can only pass along the vertical x-axis.[44]

$$m\ddot{x}(t) + c\dot{x}(t) + kx(t) = f(t) \quad (4)$$

Equation 4 states that the sum of all forces acting on the mass m should be equal to zero, with $f(t)$ representing an externally applied force, $m\ddot{x}(t)$ representing the inertial force, $c\dot{x}(t)$ representing the damping internal force, and $kx(t)$ representing the restoring force. Where, $x(t)$ is the position of the mass. Changing the domain to that of Laplace [44]gives,

$$Z(s)X(s) = F(s) \quad (5)$$

With $Z(s)$ the dynamic stiffness,

$$Z(s) = ms^2 + cs + k \quad (6)$$

The inverse of the dynamic stiffness equals the transfer function,

$$H(s) = \frac{1}{ms^2 + cs + k} \quad (7)$$

The poles of the system are the roots of the denominator of the transfer equation. The damping coefficient in mechanical structures is usually very small, resulting in a complex conjugate pole pair,

$$\lambda = -\sigma \pm i\omega_d, \text{ with } \sigma = -\zeta\omega_n \quad (8)$$

Where:

ζ = The damping factor

$f_d = \frac{\omega_d}{2\pi}$: damped natural frequency, with $\omega_d = \omega_n\sqrt{1 - \zeta^2}$

$f_n = \frac{\omega_n}{2\pi}$: natural frequency, with $\omega_n = \sqrt{\frac{k}{m}} = \lambda$

$$\ddot{x} + \frac{c}{m}\dot{x} + \frac{k}{m}x = 0 \quad (9)$$

where:

$$\frac{c}{m} = 2 \zeta \omega_n$$

$$\frac{k}{m} = \omega_n^2$$

The mechanism is not damped if $c=0$, and the poles become strictly imaginary. $H(i\omega)$ denotes the Frequency Response Function (FRF), which is obtained by replacing the Laplace variable s in Equation 7 with $i\omega$.

$$H(i\omega) = \frac{1}{-m\omega^2 + ic\omega + k} \quad (10)$$

We can observe that if $c = 0$, then $H(i\omega)$ will be infinity for $\omega = \sqrt{k/m}$. While only a few functional structures can be realistically modeled by a single-degree-of-freedom (SDOF) system, SDOF properties are important because those of a more complex multiple-degree-of-freedom (MDOF) system can often be expressed as the linear superposition of many SDOF characteristics[44].

2.5 Finite Element Analysis

Starting with a basic model is an excellent place to begin with, when using finite element modeling. When a mathematical model has been solved correctly, and the results have been interpreted, a more refined model can be considered to improve the accuracy of the actual system prediction. The more complicated model would have more complex response effects, but it will also be more expensive, time-consuming, and often challenging to interpret the results. Modeling necessitates a thorough understanding of the physical action of the problem to choose appropriate types of analysis. By avoiding Over refining and badly shaped elements can helps to save time and computer resource. The finite element analysis method is a numerical solution technique that divides an area into small subregions and seeks an approximate solution. The solution that satisfies the governing equations within each sub-region is much easier to find than the solution needed for the entire region. The sub-region is called as elements. The elements are put together by connecting a limited number of points on each one is called as nodes. In commercial FEA software, there are several different types of finite elements as shown in Figure 4, Figure 5 and Figure 6 [4].

It is simpler to obtain FEA results than it is to perform hand calculations using traditional theories. In theory, three-dimensional volume elements may be used to model any design. However, this is not realistic since many designs can be simplified using rational assumptions to obtain good FEA results without sacrificing accuracy.

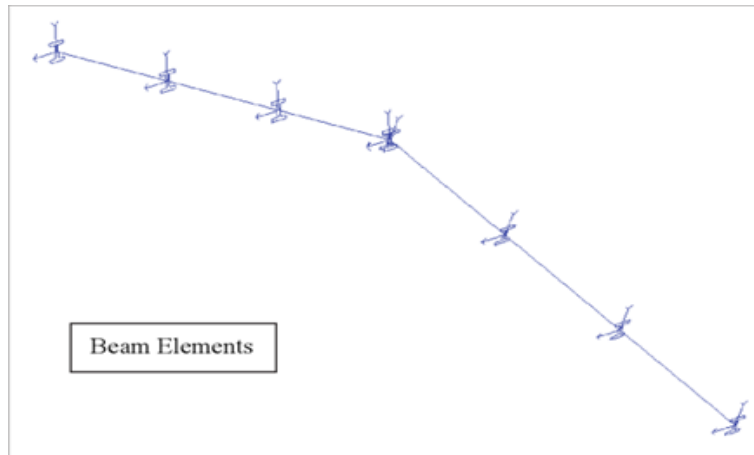


Figure 4: *One dimensional line element have trusses, beams and boundary elements [4]*

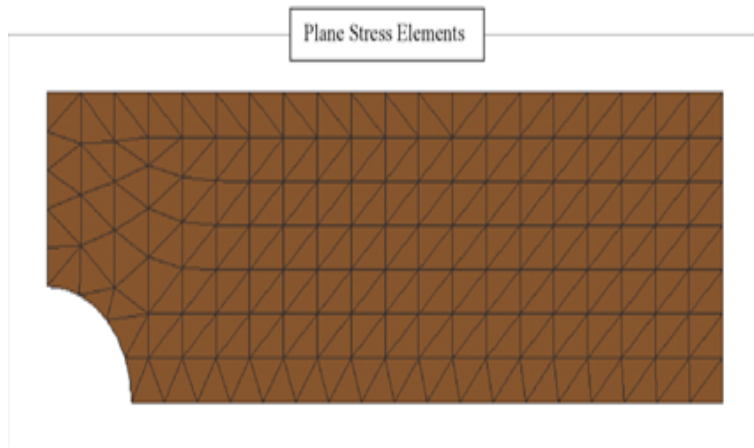


Figure 5: *Two-dimensional plane elements has plane stress, plane strain, axisymmetric, membrane and shell elements [4]*

The time and effort required to arrive at FEA solutions are significantly reduced when simpler models are used[4].

The type of finite element software used for machining analysis has a significant impact on the quality and nature of the analysis that can be done, and it provides comprehensive and efficient solutions for both routine and complex engineering problems across various industrial applications. For this project we select Abaqus as a FEM tool to perform the all the simulations[50][51]. Abaqus is a general-purpose finite element model (FEM) program that can be used to address a wide range of issues. It has three different technologies to simulate different area of problems. Abaqus/Standard is used to simulate static and low-speed dynamic events. Abaqus/Explicit is used to simulate highly nonlinear and high-speed dynamic events[52]. Abaqus/CFD is used to simulate computational fluid dynamics. Processing of the simulation depends on the keywords that are used to set up the simulation. With the help of specific axioms to model the machining operation, the user has complete control over the simulation and Abaqus does not endorse any materials, however it does enable users to customize them using a variety of models. Meshing and element types used in the

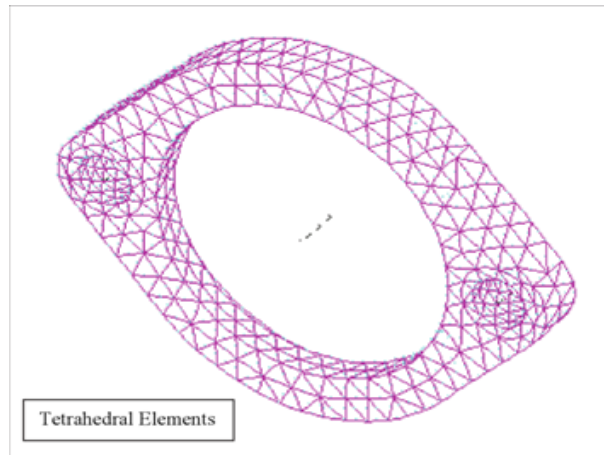


Figure 6: *Three-dimensional volume elements has tetrahedral, hexahedral and brick elements [4]*

model are also completely under the user's control. The most significant benefit of Abaqus is that it allows for detailed modeling. The user may create a very comprehensive model that describes different types of actions. The disadvantage in this program is the user must manually set several of the simulation parameters, which takes a long time to "setup" simulations[53].

3 Methodology

This project was performed in three different phases, the first of which was to reconstruct the work of T. Nazarova and her team on "*Vibration-insensitive reference cavity for an ultra-narrow-linewidth laser*"[1]. The material's mechanical properties of Yttrium Orthosilicate, which was suggested by Amin Mirzai and his team in their work on "*First-principal investigation of doping effects on mechanical and thermodynamic properties of Yttrium Orthosilicate,*"[36] were investigated in the second phase to evaluate and compare the different responses of the material, the same model, boundary, and load conditions obtained from stage one were used. The boundary condition, load, and material properties from the first two phases were used to evaluate and observe the dynamic responses of a rectangular cavity in the final stage.

The available literature was systematically explored in the first step, and the knowledge and data needed to run the simulation were gathered. Specific differences were discovered during the analysis and had to be assumed in order to operate a simulation effectively. The exact geometrical dimensions of the model used by T. Nazarova were used with the same material properties based on the data gathered[1]. Since the boundary and load conditions were not precisely defined, load and boundary conditions were varied to find the optimal location and value of the prior conditions in order to achieve the same results as T. Nazarova's work. Just a quarter of the cavity was measured using symmetric boundary conditions due to symmetry, which helped minimize the cavity's overall simulation run time.

In the second phase, one set of load and boundary conditions were finalized by consulting with the supervisors. The part dimension was kept constant as in the first phase. The material properties were changed to Yttrium Orthosilicate to study the difference in this composite material's behavior compared with the Ultra-low expansion glass, which was used in the first phase. The result of the analysis were analyzed and presented in the section below. The final step was to analyze the dynamic properties of the rectangular cavity defined to us using the same boundary and load conditions as the second phase, as well as the same material properties. Compared to the component model used in the first two stages, the rectangular cavity had a different shape and size[1][36].

The figure 7 represents the flow chart used to build the FE model. In the following sections, more information about each phase of the method is provided in greater detail.

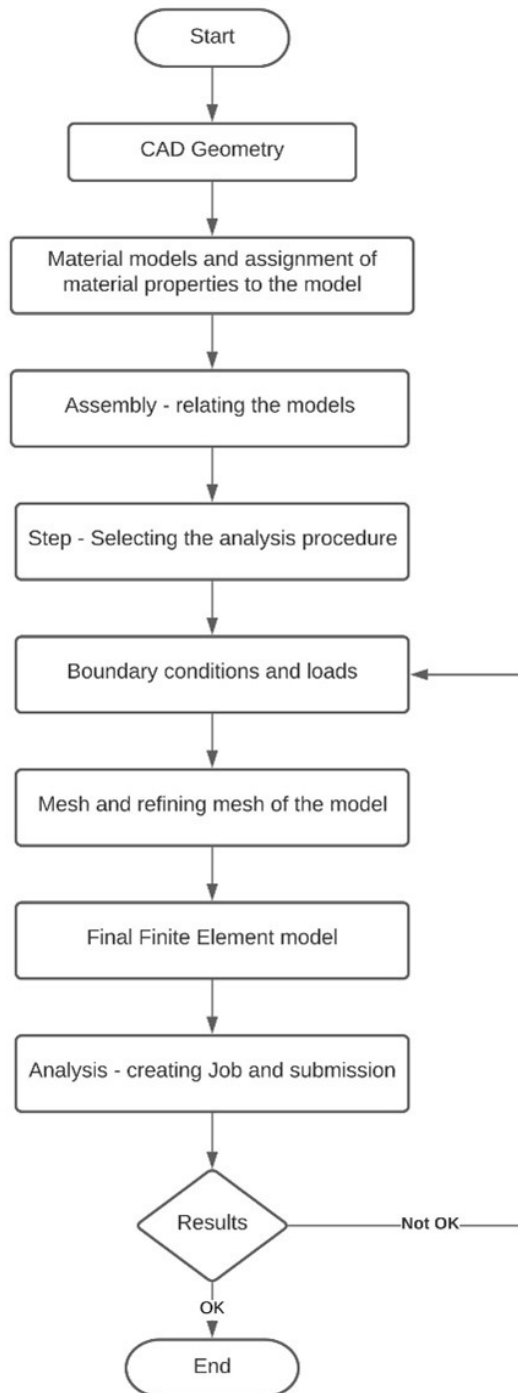


Figure 7: Working procedure used to develop the FE model

3.1 CAD Geometry

Parts are the elements that make up an Abaqus/CAE model. Each component is created, modified, and manipulated using the Part module. In this project, two models were used, each with a unique geometry. The cylindrical model was used in the first two phases of the thesis, and the rectangular model in the third phase, as described in the previous section. The modeling space was set to 3D deformable, and the base function was set to solid extrusion when creating the part.

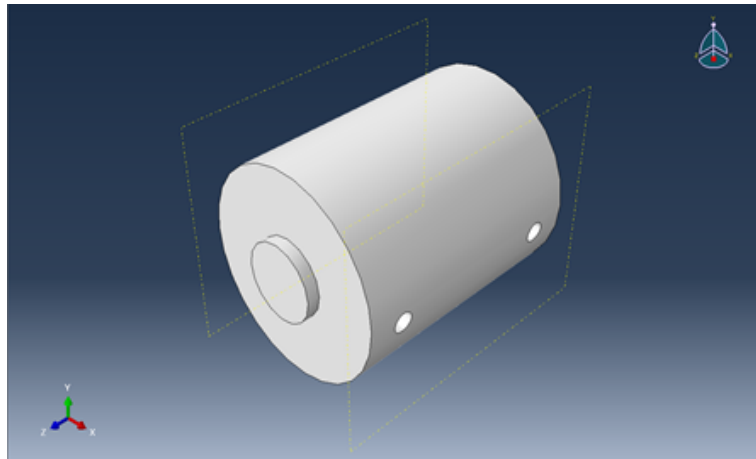


Figure 8: *Cylindrical spacer cavity model*

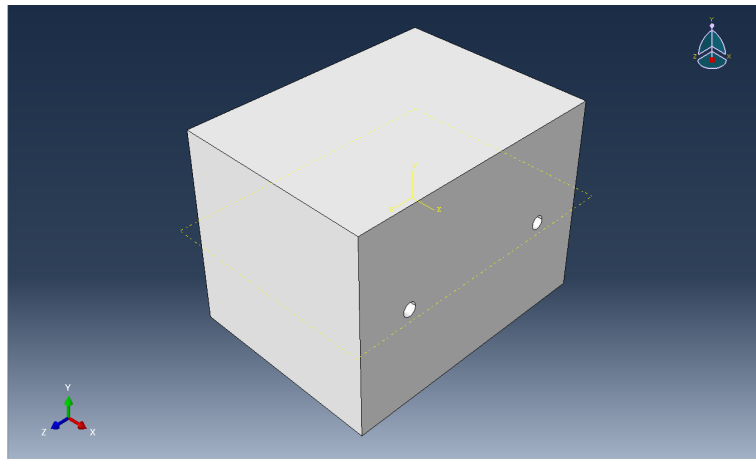


Figure 9: *Rectangular spacer cavity model*

The cylindrical spacer has a length of 0.1m and a diameter of 0.08m, as shown in Figure 8. The support holes measure 0.008 meters in diameter and 0.01 meters in depth. The support points of the cylindrical spacer are 0.07m apart and 0.035m from the center in the Z-axis. The support points are 0.0009m in the negative Y direction. The rectangular spacer cavity was used to explore the final steps of this thesis as shown in the figure 9. The rectangular spacer cavity has a height of 0.014m and a width of 0.015m, with a length of 0.02m. The support holes have a diameter

of 0.001m and a depth of 0.002m. The support holes have a diameter of 0.001m and a depth of 0.002m. The support holes are 0.012m apart, and 0.006m from the center axis in either direction of the Z-axis and are on the symmetry axis in the Y-axis. The dimensions of the rectangular spacer cavity was suggested by the supervisors as the rectangular model is being used in the department of physics, Lund university and this is the reason for dimensional differences between two models.

3.2 Material Model

Defining materials, defining beam section profiles, defining sections, assigning sections, orientations, normals, tangents to components, and defining composite layups are all the tasks that the Property module can be used for. The materials used in this study are ultra-low expansion glass and Yttrium Orthosilicate, both of which were chosen based on the literature available to us.

Ultra-low expansion glass with a density of 2210 Kg/m³ was used in the first phase. ULE has a Poisson's ratio of 0.17 and Young's modulus of 67.6 GPa. In both the second and third phases, Yttrium Orthosilicate was used; the density of Yttrium Orthosilicate was taken to be 4440 Kg/m³, and the elastic constants are represented in the following elastic stiffness matrix C, with units in GPa.

$$C = \begin{bmatrix} 212.21 & 62.78 & 78.65 & 0 & 11.64 & 0 \\ - & 197 & 49.50 & 0 & -13.56 & 0 \\ - & - & 173.21 & 0 & -21.07 & 0 \\ - & - & - & 61.42 & 0 & 10.08 \\ - & - & - & - & 48.41 & 0 \\ - & - & - & - & - & 69.25 \end{bmatrix}$$

Following the development of the components, materials were created, and they were assigned to their respective models. Local coordinates were established for anisotropic materials, and material orientations were allocated.

3.3 Step

The splitting of the problem history into steps is a fundamental principle in Abaqus. Any suitable phase of the past can be a thermal transient, a creeping hold, a dynamic transient, and so on is referred to as a step. A step can be as simple as static analysis of a load shift from one magnitude to another in Abaqus/Standard. Since the aim was to research the system's quasi-static deformation and natural frequencies, we set the step to Dynamic, Explicit, Automatic Increment, and Nilgeom - ON, as shown in the Figure 10.

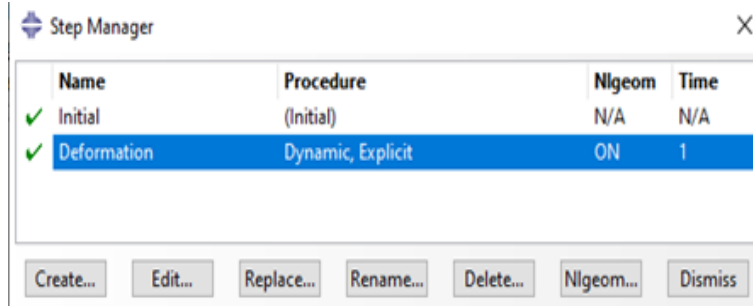


Figure 10: Step instance

3.4 Boundary and load conditions

After assigning the material properties to the model and selecting the required step based on the type of simulation to run, the next important step is to apply boundary conditions and loads to the designated face or plane of the model. Boundary conditions are applied to restrict the model’s movement from the forces or loads applied externally or due to self-driven load in the model. These boundary conditions are directions dependent factors that should be carefully assigned to the required surface or plane of the model. A minor unnecessary constraint leads to a more considerable simulation time variation and inappropriate results.

As mentions previously, all the data are extracted from the given paper to recreate the model. According to the article[1], the model should be constraining or supported at four supporting holes drilled on the symmetrical axis of the cavity or model. It is also clearly mentioned that the whole supporting holes are not entirely constrained in all directions. But the specification of the boundary conditions is not mentioned in the paper. This leads to an increase in the number of simulations to determine the proper constraints of the face and its directions of the model.

We ran several simulations using the limited data in the paper for boundary conditions by adjusting constrained faces and directions within the supporting holes. The different boundary conditions are considered based on our knowledge, along with the suggestions from our supervisors. After every simulation, the results were carefully monitored and discussed with our supervisor to develop better boundary conditions to give relevant results. Each simulation with varying boundary conditions is finite due to the long simulation time, ranging from 12 to 48 hours. A result that is nearly similar to the one discussed in the paper, is obtained after several simulations. The upper half of the inner circle was constrained normal to the surface by the boundary conditions used to obtain this result, i.e., $XSYMM(U1=UR1=UR2=0)$, which is shown in the figure 11 (Area marked with red). The load is also tracked, in addition to the boundary conditions, by applying it to different phases of the model. As seen in the figure 11, the considered load is a 10 m/s^2 acceleration in upward Y-direction acting on the mirrors (represented by yellow lines).

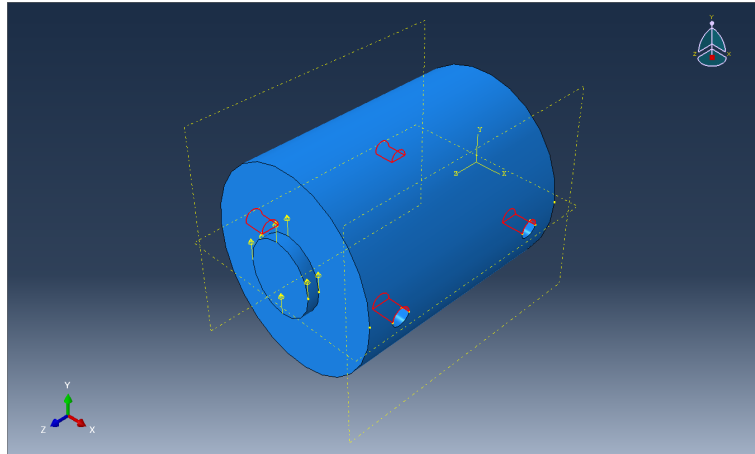


Figure 11: *Applied load and boundary conditions for cylindrical model*

The boundary conditions and load from the simulation that produced results that are about 90 percent close to the results in the reference paper are taken into account for subsequent simulations. The geometry and material properties are the only things that are altered. The modified geometry is shown in the figure 12, for the same boundary conditions and load.

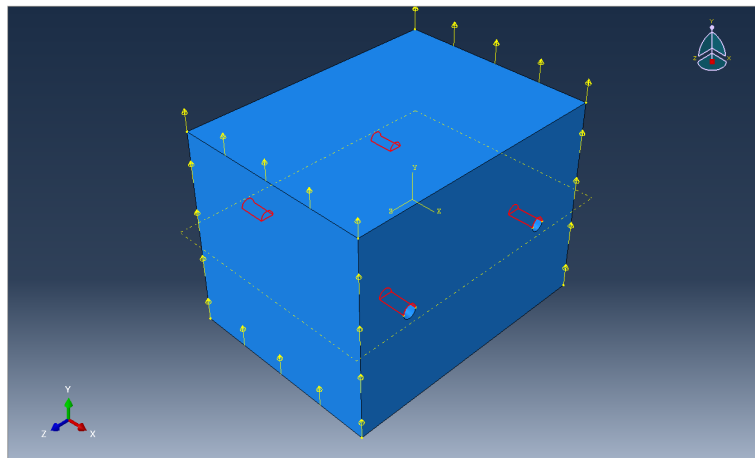


Figure 12: *Applied load and boundary conditions for rectangular model*

3.5 Meshing of the model

The Mesh module includes tools for creating meshes from parts and assemblies generated in Abaqus/CAE. The Mesh module also contains functions for verifying an existing mesh. Due to the geometry's complexity, some approximations and geometry clean-up were needed to mesh the model as precisely as possible. Even though a mesh with many elements produces more accurate results than a rough mesh, it was essential to mesh irregularly. This is because, holes in the geometry rapidly increase the number of elements required, lowering the study's computational cost and

jeopardizing the model's stability. The mesh was given a tetrahedron shape to avoid affecting the geometry of the holes. The meshed models for both the geometries are shown in figure 13 and figure 14.

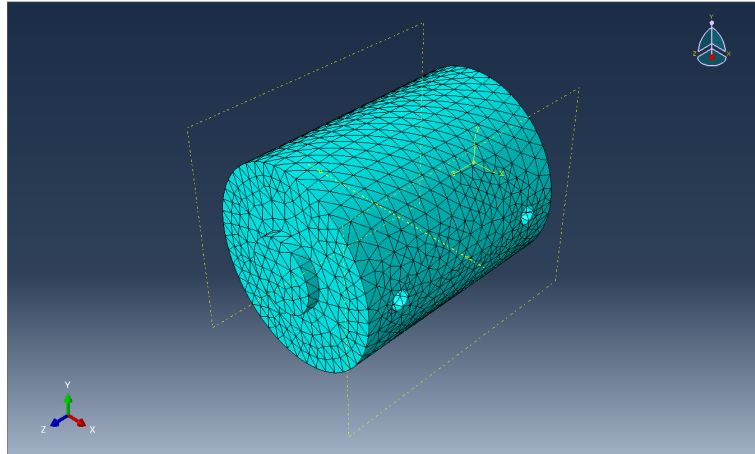


Figure 13: *Meshed image of cylindrical model*

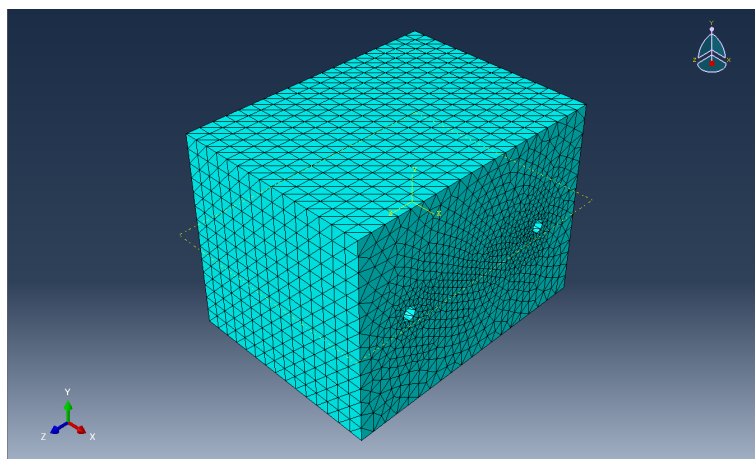


Figure 14: *Meshed image of rectangular model*

4 Results

There are three sections in the simulated results. Section 4.1 presents the results of a cylindrical model simulation with two different material properties. Section 4.2 shows the results of a rectangular model simulation with two different material properties, and section 4.3 presents the modal analysis results for both models. In the chapter 5, these results are contrasted and explained in detail.

4.1 Simulation of cylindrical model

Because of the symmetry, just a half of the model is shown below. This section is broken down further into two subsections. Section 4.1.1 shows the results of a cylindrical model simulation with isotropic material properties, while section 4.1.2 shows the results of a cylindrical model simulation with anisotropic material values, these material properties are described in section 3.2. Legends represent the stresses with corresponding color code in the figures.

4.1.1 Cylindrical model with isotropic material properties

The below figures shows the deformation and stress distributions on the cylindrical model with isotropic material properties. The exhibited data have been scaled for better comparison and analysis.

From the figure 15, for the deformation occurring in X-direction, it is evident that the magnitude of deformation is distributed throughout the cylindrical cavity. As we have considered only half of the cavity due to its symmetrical property, it is probable to conclude that the other half of the cavity will also have identical distribution of load and deformation. The obtained results in figure 15 suggests that when the load conditions are applied in positive Y-direction, both compression and expansion takes place at the cylindrical cavity. The scaling of the magnitude of deformation is done in such a way, that the green part of the cavity holds the ideal or minimal deformation, whereas when expansion takes place, the magnitude of deformation increases positively, which is represented with yellow to red. Similarly, it is evident that the blue part of the cavity denotes the compression that takes place at the bottom part of the cavity, gradually increasing from centre of the cavity towards the circumference of the cylindrical cavity.

From figure 16, when the results are obtained for deformation in Z-direction, it is evident that expansion takes place at the bottom part of the cavity, with the maximum magnitude of $1.55e-11$ m. Whereas, compression takes place at the top part of the cavity, with the maximum magnitude of $1.55e-11$ m.

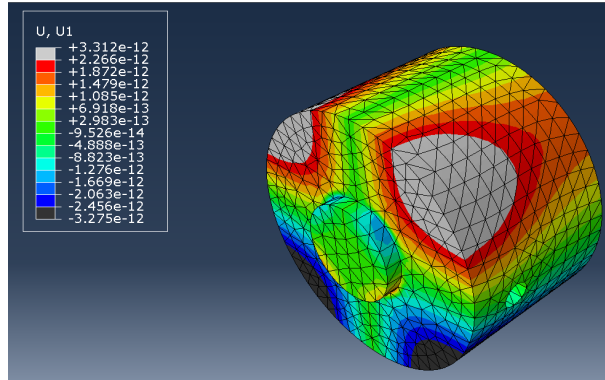


Figure 15: Simulated deformation in X-direction under an 0.1 m/s^2 acceleration in Y-direction

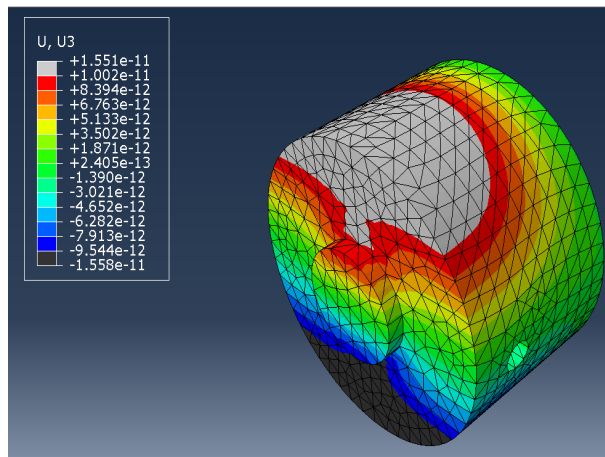


Figure 16: Simulated deformation in Z-direction under an 0.1 m/s^2 acceleration in Y-direction

Figure 17 shows the von-mises stress distribution when the cavity is under 0.1 m/s^2 acceleration in Y-direction. The stress component clearly shows that the stress is more concentrated at the mirror. The results obtained are logical and reliable because, it is obvious that the stresses will act at the interference of the mirror and cavity. From figure 16, we can see that the magnitude of the maximum stress is 553.8 N/m^2 at the interference of the mirror and cavity and the stress is distributed only up to a certain extend in cavity with a minimum magnitude of 41.67 N/m^2 .

Figure 18 shows the maximum principal stress distribution under an acceleration of 0.1 m/s^2 in Y-direction. The results obtained shows us that the stress is concentrated at the interference of mirror and cavity with a maximum magnitude of 464.7 N/m^2 . The load is distributed to the cavity which decreases gradually towards the outer part of the cavity. The minimum magnitude of stress recorded is a compressive stress of 5.35 N/m^2

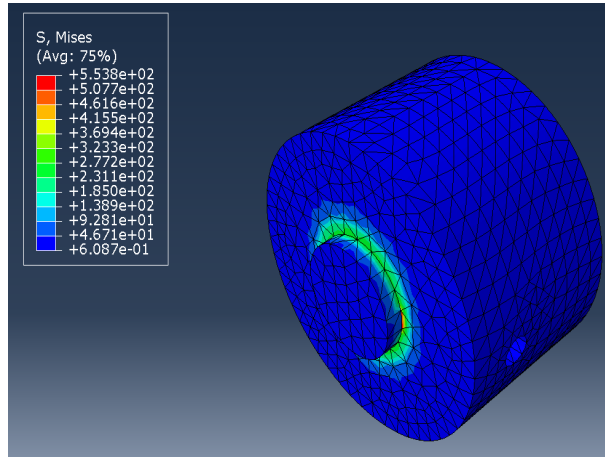


Figure 17: Von-Mises stress distribution under an 0.1 m/s² acceleration in Y-direction

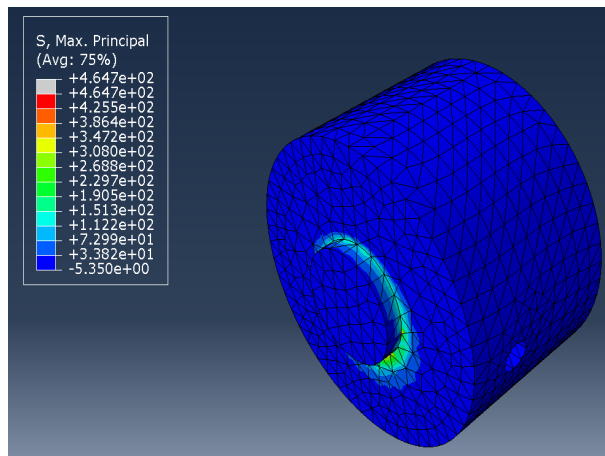


Figure 18: Maximum principal stress distribution under an 0.1 m/s² acceleration in Y-direction

4.1.2 Cylindrical model with anisotropic material properties

The below figures shows the deformation and stress distributions on the cylindrical model with anisotropic material properties. The exhibited data have been scaled for better comparison and analysis. There were three orientation conditions analyzed. In the first condition, the stacking direction is element isoparametric direction Z-axis . Figure 19 shows the deformation that takes place in X-direction, when an acceleration of 0.1 m/s² is applied. From the results obtained we can see that the compression takes place at the bottom part of the cavity, with a maximum magnitude of 4.36e-12 m, whereas expansion takes place at the top part of cavity with a maximum magnitude of 3.429e-12 m .

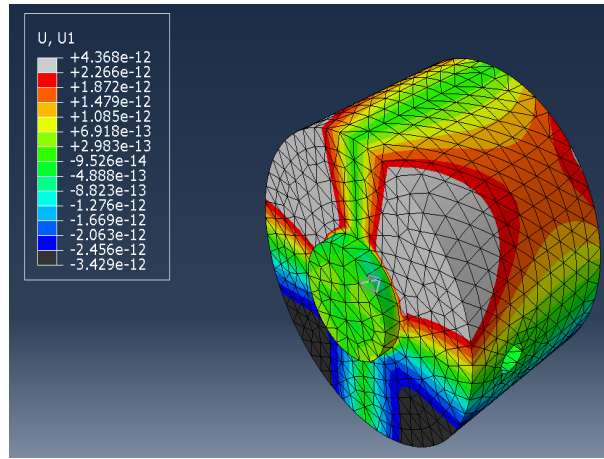


Figure 19: Simulated deformation in X-direction under an 0.1 m/s² acceleration in Y-direction

From figure 20, we can see the deformation in Z-direction under 0.1 m/s². The results obtained clearly shows that extension takes place at the bottom part of the cavity with a maximum deformation of 1.31e-11 m. Whereas, at the top of the cavity, we note compression of magnitude 1.365e-11 m.

From figure 21 we can identify the von-mises stress acting on the optical cavity, with an acceleration of 0.1 m/s² applied on the mirror. We can clearly see that the stress is distributed evenly around the interference region of the mirror and cavity. With a maximum stress of 1267 N/m². The stress gradually decreases towards the circumference of the cavity.

Figure 22 shows the maximum principal stress acting on the optical cavity when subjected to an acceleration load of 0.1 m/s². From the results obtained we can deduce that the stress is distributed unevenly around the interference zone of mirror and cavity. In this case, we can identify both compressive and tensile stress that acts upon the cavity, with a maximum magnitude of 1052 N/m² for tensile stress and a maximum compressive stress of 21.9 N/m².

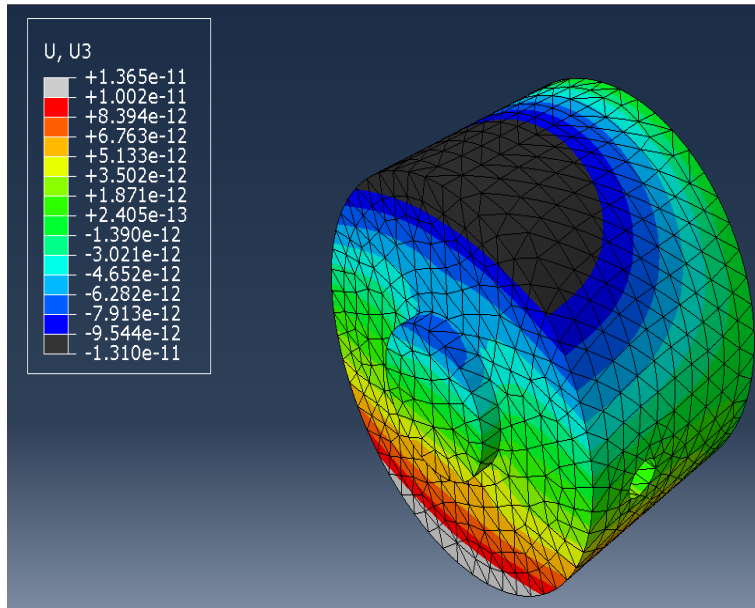


Figure 20: Simulated deformation in Z-direction under an 0.1 m/s² acceleration in Y-direction

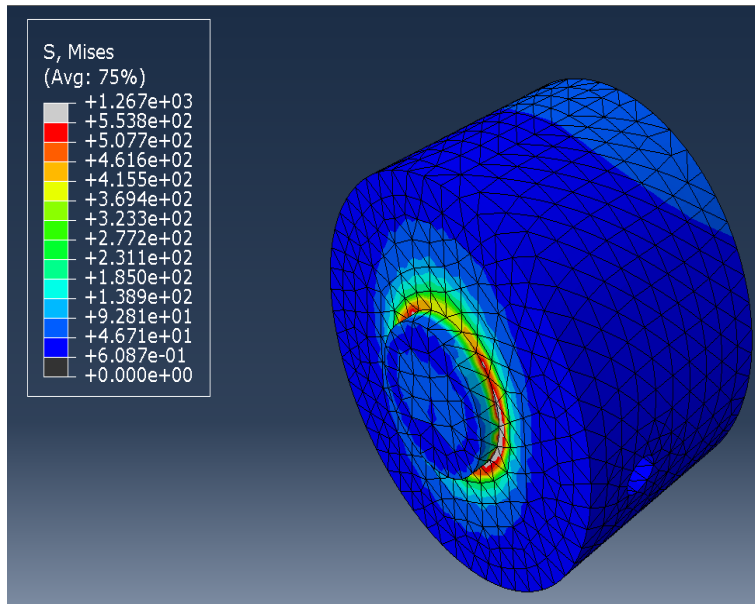


Figure 21: Von-Mises stress distribution under an 0.1 m/s² acceleration in Y-direction

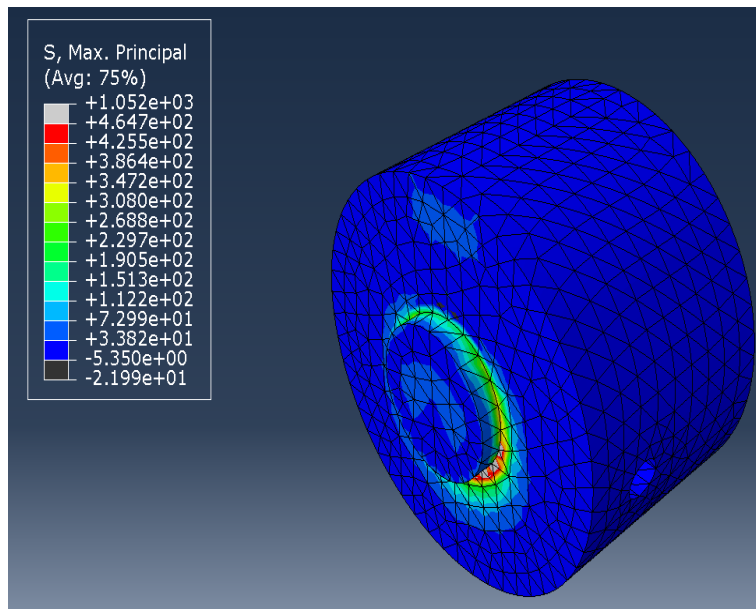


Figure 22: *Maximum principal stress distribution under an 0.1 m/s² acceleration in Y-direction*

In the second condition, the stacking direction is element isoparametric direction Z-axis with additional rotation of 90 degrees with respect to Y-axis of orientation is considered. The figure 23, figure 24, figure 25 and figure 26 shows the simulated results of cylindrical anisotropic model of second condition.

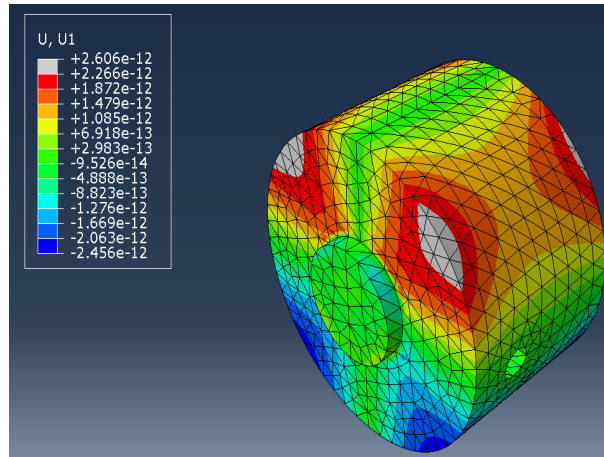


Figure 23: Simulated deformation in X-direction under an 0.1 m/s^2 acceleration in Y-direction with 90 degrees additional rotation of orientation

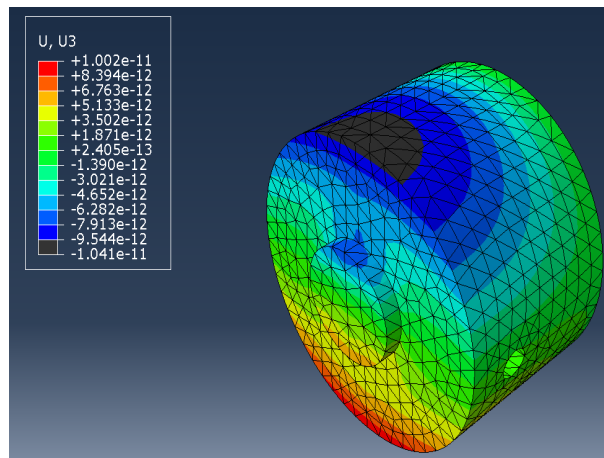


Figure 24: Simulated deformation in Z-direction under an 0.1 m/s^2 acceleration in Y-direction with 90 degrees additional rotation of orientation

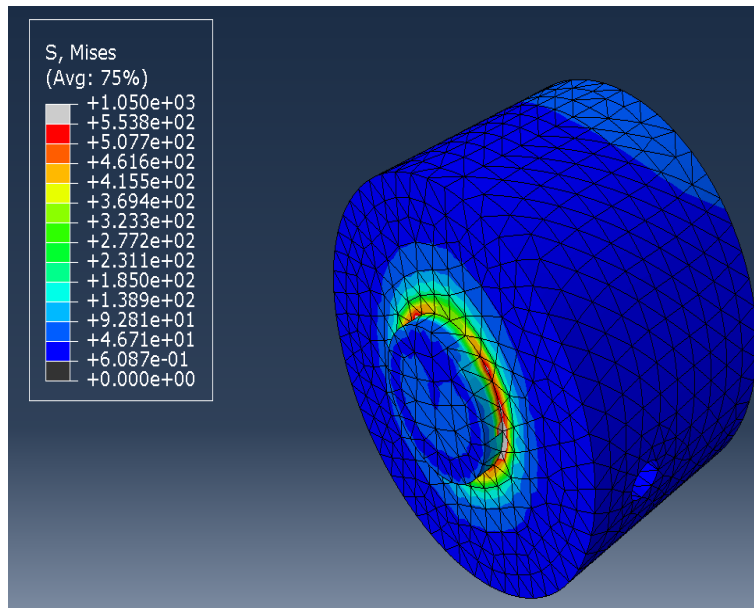


Figure 25: Von-Mises stress distribution under an 0.1 m/s^2 acceleration in Y-direction with 90 degrees additional rotation of orientation

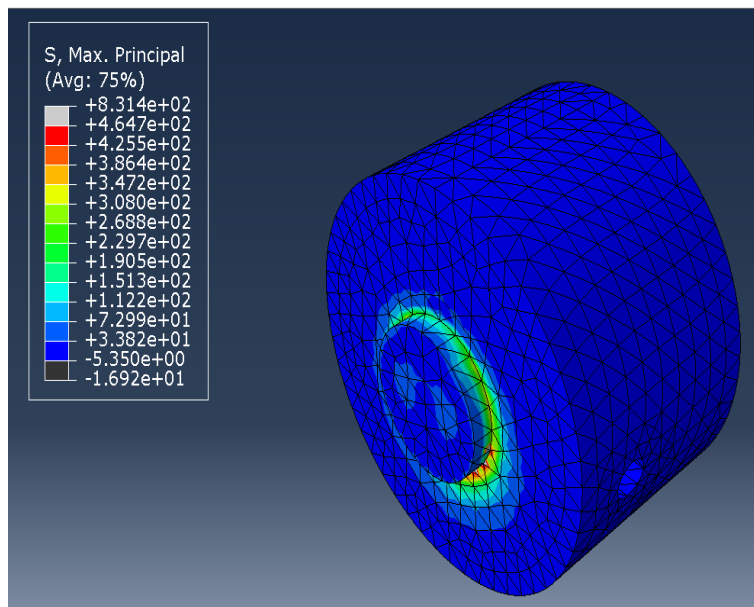


Figure 26: Maximum principal stress distribution under an 0.1 m/s^2 acceleration in Y-direction with 90 degrees additional rotation of orientation

In the third condition, the stacking direction is element isoparametric direction Z-axis with additional rotation of 270 degrees with respect to Y-axis of orientation is considered. The figure 27, figure 28, figure 29 and figure 30 shows the simulated results of cylindrical anisotropic model of third condition.

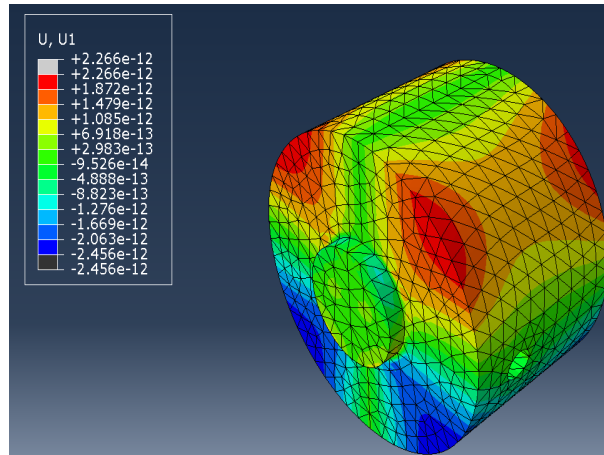


Figure 27: Simulated deformation in X-direction under an 0.1 m/s^2 acceleration in Y-direction with 270 degrees additional rotation of orientation

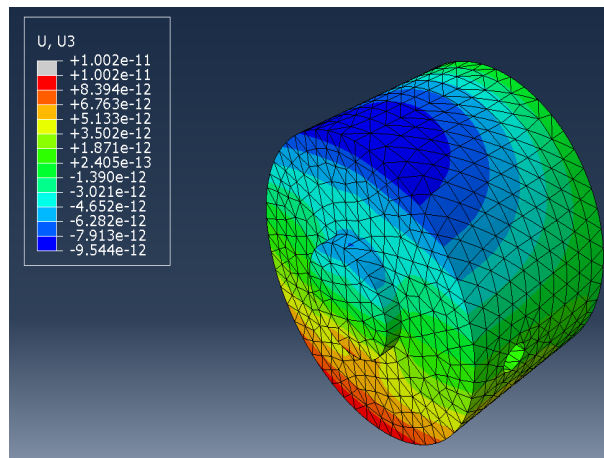


Figure 28: Simulated deformation in Z-direction under an 0.1 m/s^2 acceleration in Y-direction with 270 degrees additional rotation of orientation

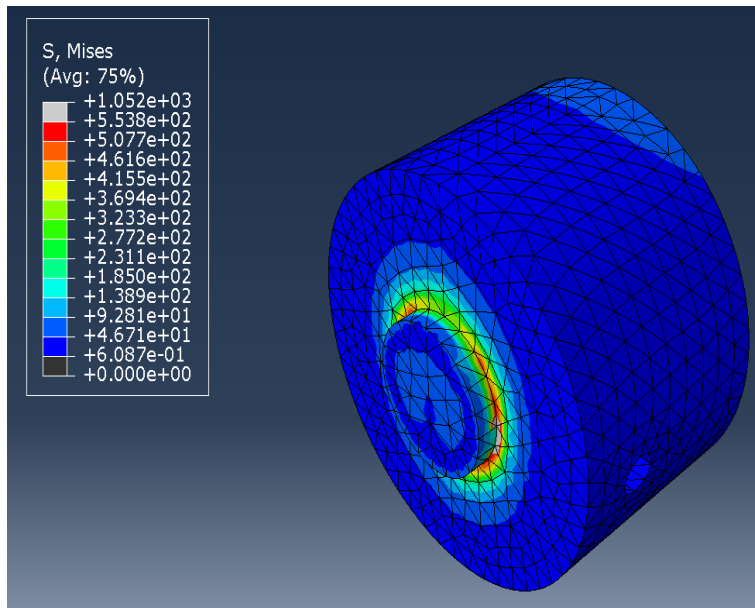


Figure 29: Von-Mises stress distribution under an 0.1 m/s^2 acceleration in Y-direction with 270 degrees additional rotation of orientation

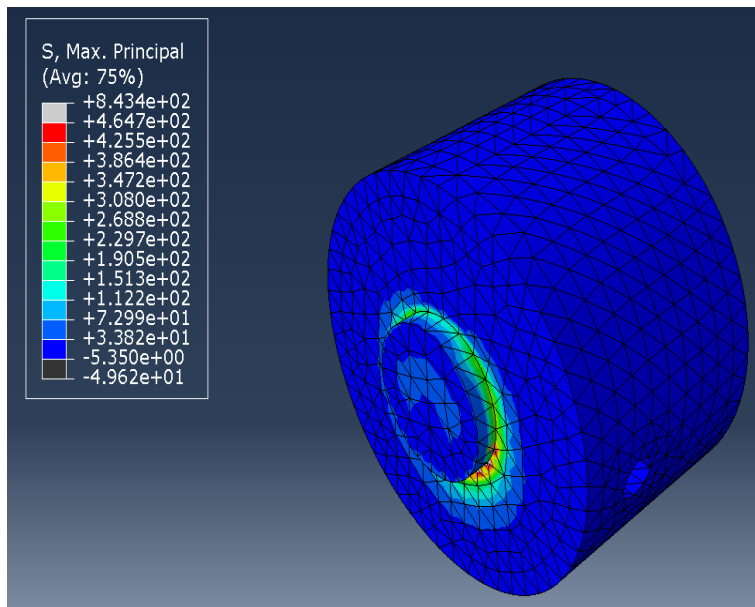


Figure 30: Maximum principal stress distribution under an 0.1 m/s^2 acceleration in Y-direction with 270 degrees additional rotation of orientation

4.2 Simulation of Rectangular model

This section is also broken down further into two subsections. Section 4.2.1 shows the results of a rectangular model simulation with isotropic material properties, while section 4.2.2 shows the results of a rectangular model simulation with anisotropic material values, these material properties are described in section 3.2. However, due to time constraints, the material properties of the rectangular models were scaled down by nine orders of negative magnitude. which saved about seventy percent of the simulation time for each simulation. Legends represent the stresses with corresponding color code in the figures.

4.2.1 Rectangular model with isotropic material properties

The figure 31, figure 32, figure 33 and figure 34 shows the deformation and stress distributions on the rectangular model with isotropic material properties. The exhibited data have been scaled for better comparison and analysis.

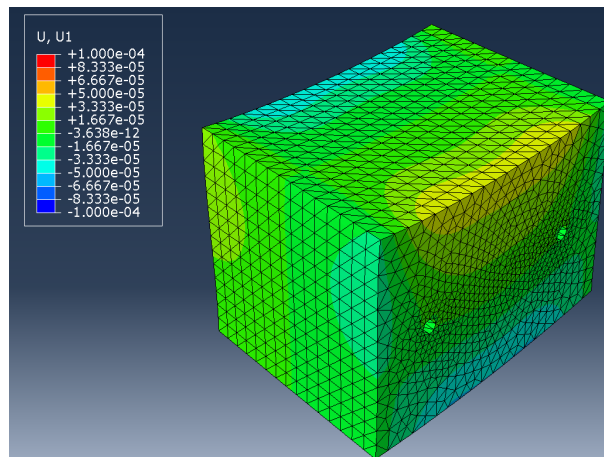


Figure 31: Simulated deformation in X-direction under an 0.1 m/s^2 acceleration in Y-direction

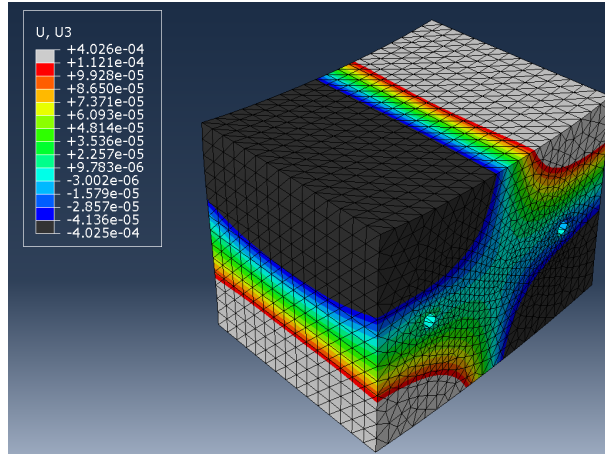


Figure 32: Simulated deformation in Z-direction under an 0.1 m/s^2 acceleration in Y-direction

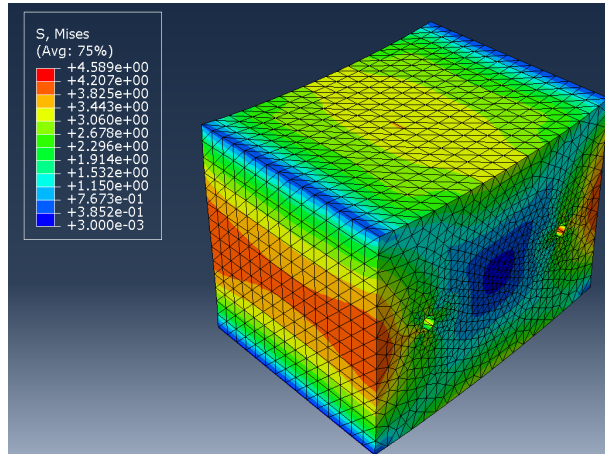


Figure 33: Von-Mises stress distribution under an 0.1 m/s^2 acceleration in Y-direction

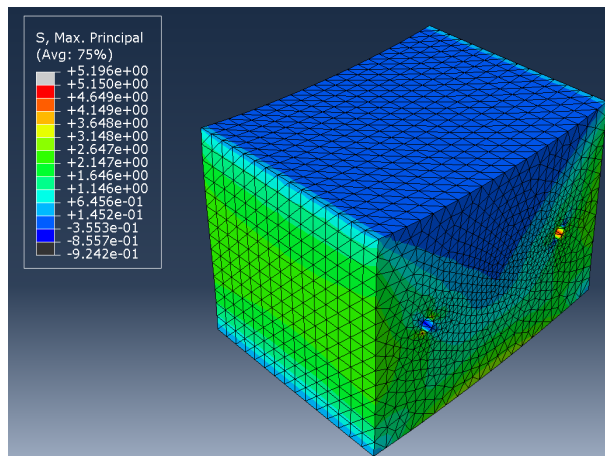


Figure 34: Maximum principal stress distribution under an 0.1 m/s^2 acceleration in Y-direction

4.2.2 Rectangular model with anisotropic material properties

The figure 35, figure 36, figure 37 and figure 38 shows the deformation and stress distributions on the rectangular model with anisotropic material properties. The exhibited data have been scaled for better comparison and analysis. There were three orientation conditions analyzed. In the first condition, the stacking direction is element isoparametric direction Z-axis.

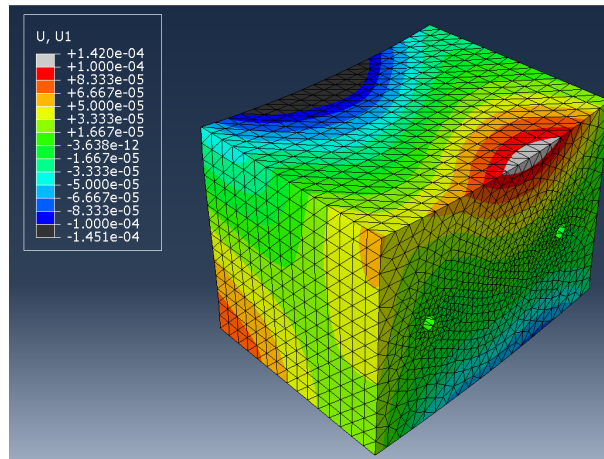


Figure 35: Simulated deformation in X-direction under an 0.1 m/s^2 acceleration in Y-direction

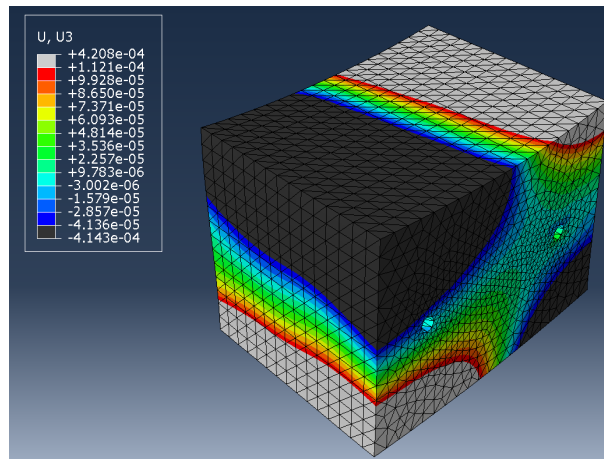


Figure 36: Simulated deformation in Z-direction under an 0.1 m/s^2 acceleration in Y-direction

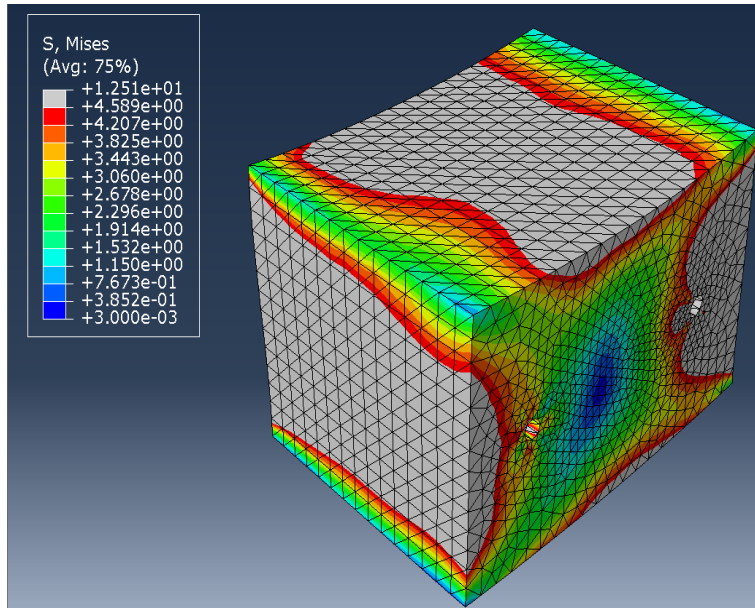


Figure 37: Von-Mises stress distribution under an 0.1 m/s² acceleration in Y-direction

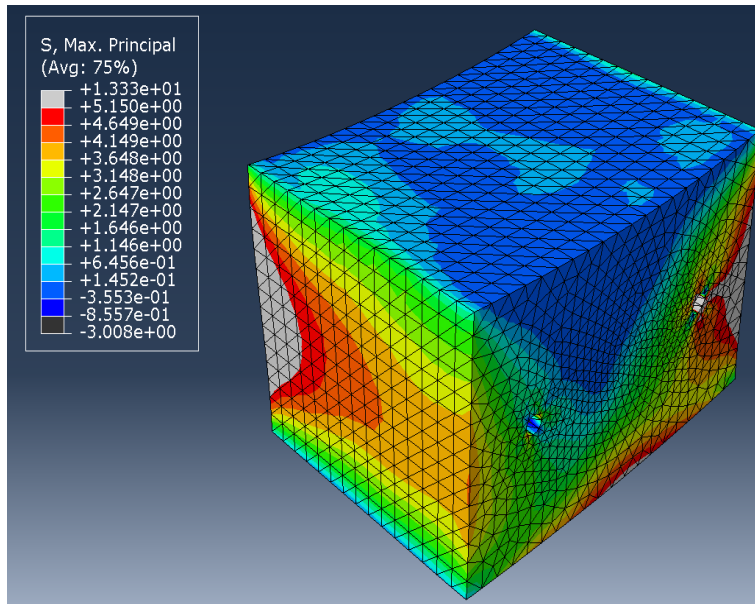


Figure 38: Maximum principal stress distribution under an 0.1 m/s² acceleration in Y-direction

In the second condition, the stacking direction is element isoparametric direction Z-axis with additional rotation of 90 degrees with respect to Y-axis of orientation is considered. The figure 39, figure 40, figure 41 and figure 42 shows the simulated results of rectangular anisotropic model of second condition.

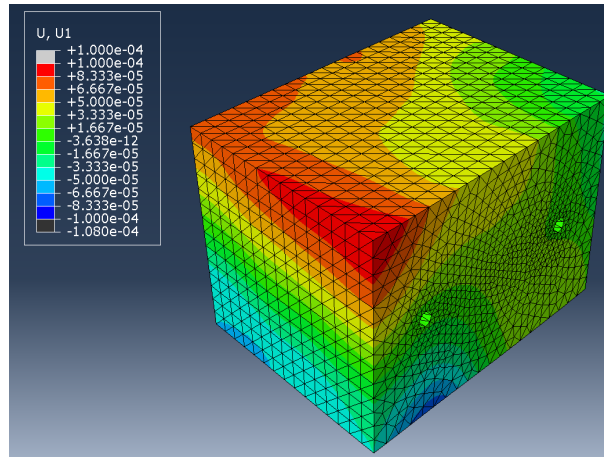


Figure 39: Simulated deformation in X-direction under an 0.1 m/s² acceleration in Y-direction with 90 degrees additional rotation of orientation

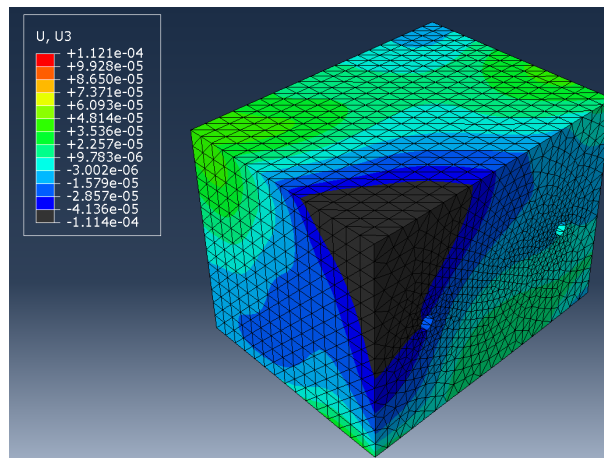


Figure 40: Simulated deformation in Z-direction under an 0.1 m/s² acceleration in Y-direction with 90 degrees additional rotation of orientation

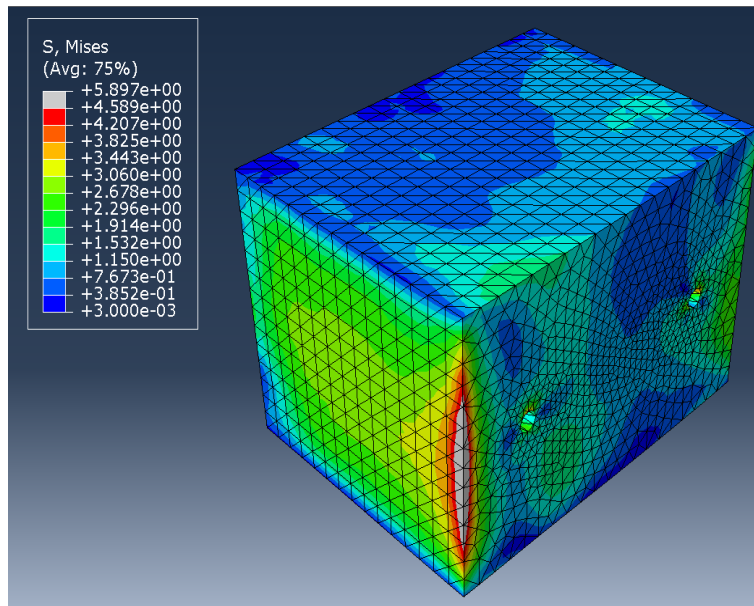


Figure 41: Von-Mises stress distribution under an 0.1 m/s^2 acceleration in Y-direction with 90 degrees additional rotation of orientation

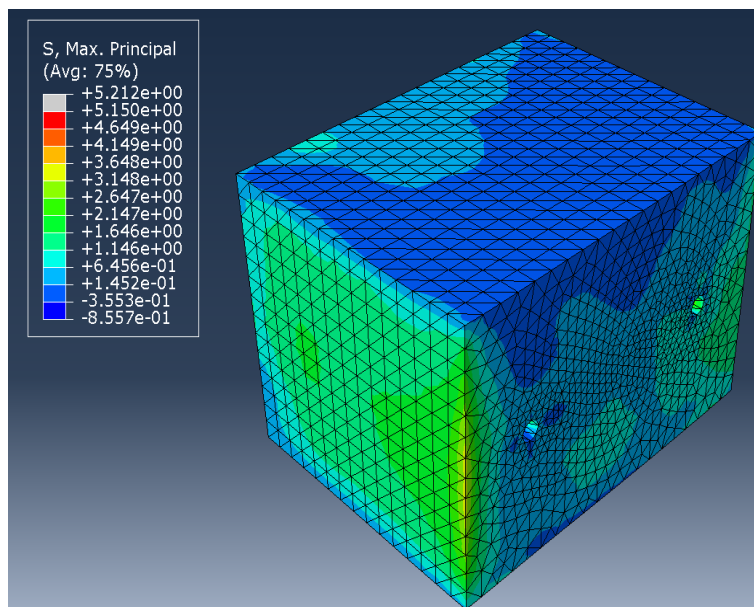


Figure 42: Maximum principal stress distribution under an 0.1 m/s^2 acceleration in Y-direction with 90 degrees additional rotation of orientation

In the third condition, the stacking direction is element isoparametric direction Z-axis with additional rotation of 270 degrees with respect to Y-axis of orientation is considered. The figure 43, figure 44, figure 45 and figure 46 shows the simulated results of rectangular anisotropic model of third condition.

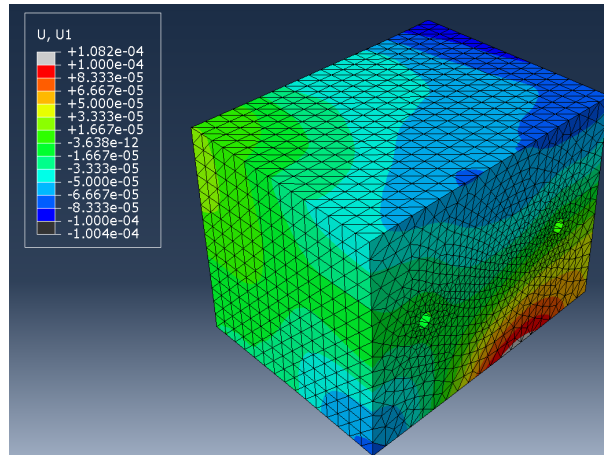


Figure 43: Simulated deformation in X-direction under an 0.1 m/s^2 acceleration in Y-direction with 270 degrees additional rotation of orientation

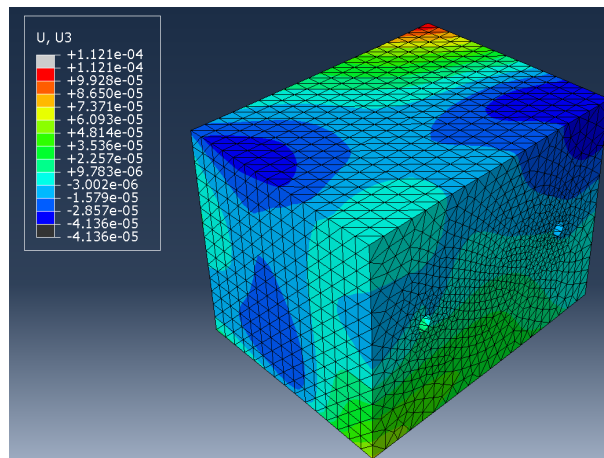


Figure 44: Simulated deformation in Z-direction under an 0.1 m/s^2 acceleration in Y-direction with 270 degrees additional rotation of orientation

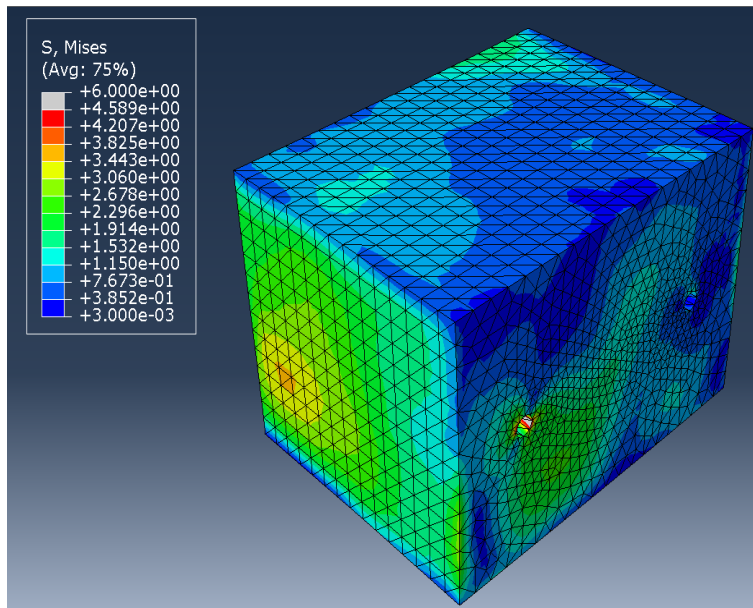


Figure 45: Von-Mises stress distribution under an 0.1 m/s^2 acceleration in Y -direction with 270 degrees additional rotation of orientation

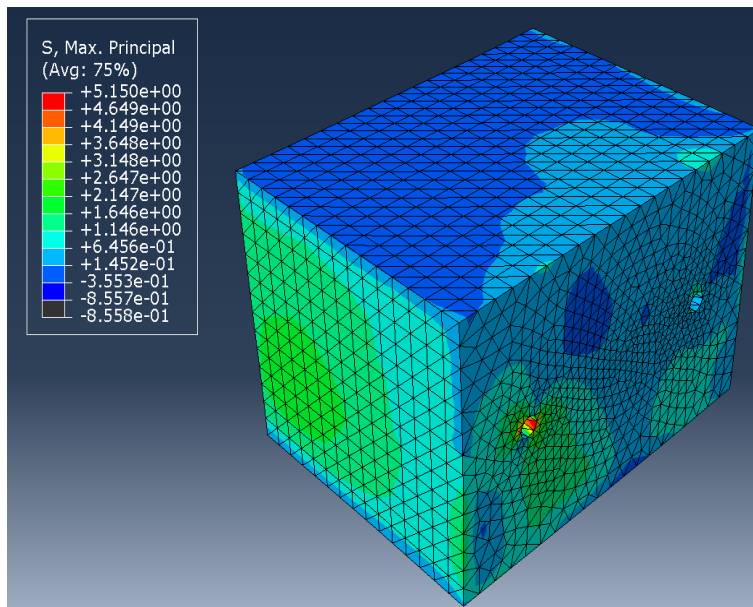


Figure 46: Maximum principal stress distribution under an 0.1 m/s^2 acceleration in Y -direction with 270 degrees additional rotation of orientation

4.3 Modal analysis

The modal analysis results on isotropic and anisotropic material properties of both the cylindrical and rectangular models are presented in this section. Each mode shape corresponds to a natural frequency, and the mode shape represents the displacement behavior. A mode of vibration is distinguished by its modal frequency and mode shape. The mode shape is determined by the surface shape as well as the boundary conditions. Modal analysis is divided into two sections. The modal analysis of a cylindrical model with two different material properties is presented in Section 4.3.1. The modal analysis of a rectangular with two different material properties is shown in Section 4.3.2. For better understanding both deformed and undeformed contours are plotted below.

4.3.1 Modal analysis of cylindrical model with isotropic material properties

The first ten natural frequencies of the cylindrical model with isotropic material properties are depicted in Figure 47. Figure 48 depicts the displacement of these ten natural frequencies as mode shapes. From the modal analysis conducted for an isotropic material, we can identify 10 different frequencies that are inadequate for the particular model. From figure 47, we can extract the frequency range, namely, 20391 to 47168 cycles/time. These frequencies range, as suggested from modal analysis produces the worst conditions for vibrations when it matches the loading frequency, as the model starts to resonate due to incompatible frequency conditions.

0	Increment	0: Base State
1	Mode	1: Value = 5.29059E-05 Freq = 1.15764E-03 (cycles/time)
2	Mode	2: Value = 1.64156E+10 Freq = 20391. (cycles/time)
3	Mode	3: Value = 2.82224E+10 Freq = 26737. (cycles/time)
4	Mode	4: Value = 4.24009E+10 Freq = 32772. (cycles/time)
5	Mode	5: Value = 5.18067E+10 Freq = 36225. (cycles/time)
6	Mode	6: Value = 5.67394E+10 Freq = 37911. (cycles/time)
7	Mode	7: Value = 6.03819E+10 Freq = 39109. (cycles/time)
8	Mode	8: Value = 6.91892E+10 Freq = 41864. (cycles/time)
9	Mode	9: Value = 8.49606E+10 Freq = 46390. (cycles/time)
10	Mode	10: Value = 8.78334E+10 Freq = 47168. (cycles/time)

Figure 47: First 10 mode Natural frequencies (f_n) of the isotropic cylindrical model

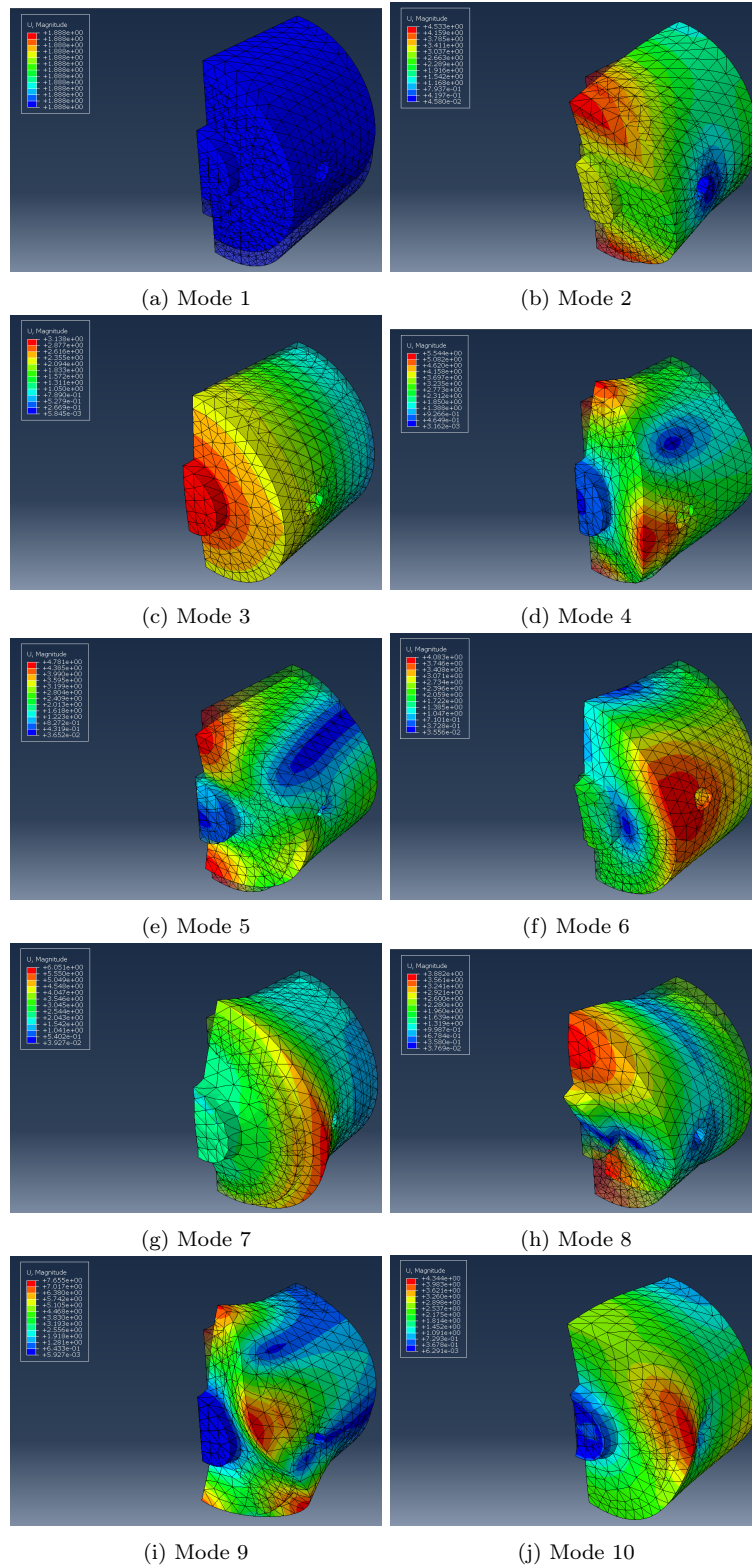


Figure 48: *Initial 10 modes of frequencies of isotropic cylindrical model*

Cylindrical model with anisotropic material properties with the stacking direction in element isoparametric direction Z-axis. From the modal analysis conducted for an anisotropic material, we can obtain the inadequate frequencies for the particular model. For the optical cavity that undergoes severe vibration due to high frequencies, it is absolutely crucial to identify the suitable loading conditions.

0	Increment	0: Base State
1	Mode	1: Value = -1.19295E-04 Freq = 0.0000 (cycles/time)
2	Mode	2: Value = -8.10597E-05 Freq = 0.0000 (cycles/time)
3	Mode	3: Value = -3.04567E-05 Freq = 0.0000 (cycles/time)
4	Mode	4: Value = 3.18760E-05 Freq = 8.98571E-04 (cycles/time)
5	Mode	5: Value = 8.17389E-05 Freq = 1.43891E-03 (cycles/time)
6	Mode	6: Value = 1.26932E-04 Freq = 1.79310E-03 (cycles/time)
7	Mode	7: Value = 1.85803E-04 Freq = 2.16943E-03 (cycles/time)
8	Mode	8: Value = 1.71213E+10 Freq = 20825. (cycles/time)
9	Mode	9: Value = 1.95782E+10 Freq = 22269. (cycles/time)
10	Mode	10: Value = 2.76855E+10 Freq = 26482. (cycles/time)

Figure 49: First 10 mode Natural frequencies (f_n) of the anisotropic cylindrical model

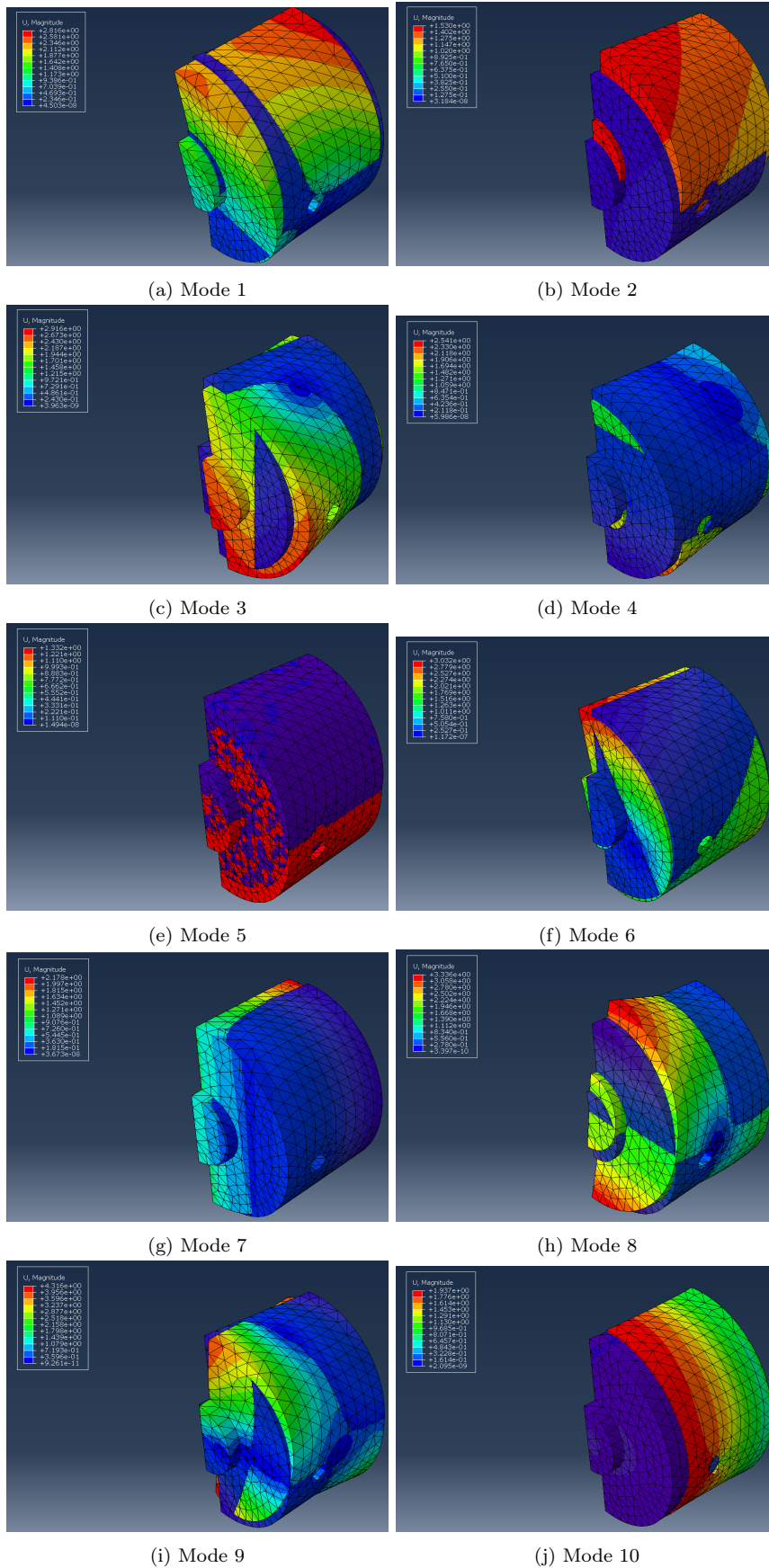


Figure 50: Initial 10 modes of frequencies of anisotropic cylindrical model

Cylindrical model with anisotropic material properties with the stacking direction in element isoparametric direction Z-axis and additional rotation of 90 degrees with respect to Y-axis of orientation is considered. For the modal analysis conducted for an anisotropic material with a additional rotation of 90 degrees with respect to Y-axis. Any frequency that is used in this particular frequency, will result in resonance inside the cavity. Even though the minimum frequency is similar to previous orientation, it is crucial to identify even the slightest of variations for all the possible orientations of the anisotropic material.

0	Increment	0: Base State
1	Mode	1: Value = -7.01551E-05 Freq = 0.0000 (cycles/time)
2	Mode	2: Value = -6.12674E-05 Freq = 0.0000 (cycles/time)
3	Mode	3: Value = 7.79203E-06 Freq = 4.44268E-04 (cycles/time)
4	Mode	4: Value = 2.70692E-05 Freq = 8.28053E-04 (cycles/time)
5	Mode	5: Value = 1.33461E-04 Freq = 1.83864E-03 (cycles/time)
6	Mode	6: Value = 1.39264E-04 Freq = 1.87819E-03 (cycles/time)
7	Mode	7: Value = 2.31485E-04 Freq = 2.42148E-03 (cycles/time)
8	Mode	8: Value = 1.52982E+10 Freq = 19685. (cycles/time)
9	Mode	9: Value = 1.87187E+10 Freq = 21775. (cycles/time)
10	Mode	10: Value = 2.67061E+10 Freq = 26009. (cycles/time)

Figure 51: First 10 mode Natural frequencies(f_n) of the anisotropic cylindrical model

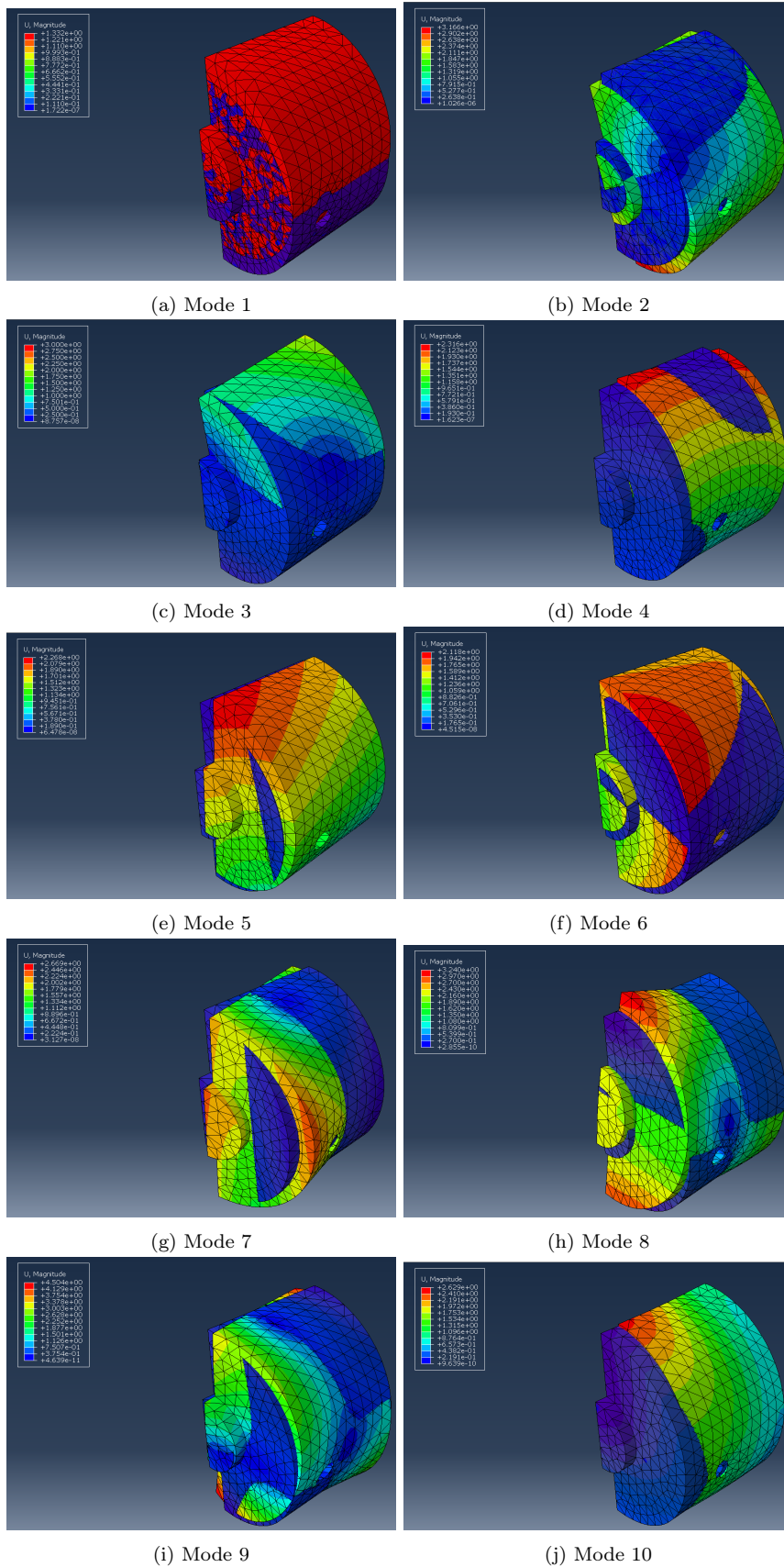


Figure 52: Initial 10 modes of frequencies of anisotropic cylindrical model

Cylindrical model with anisotropic material properties with the stacking direction in element isoparametric direction Z-axis and additional rotation of 270 degrees with respect to Y-axis of orientation is considered.

0	Increment	0: Base State
1	Mode	1: Value = -7.20942E-05 Freq = 0.0000 (cycles/time)
2	Mode	2: Value = -5.31744E-06 Freq = 0.0000 (cycles/time)
3	Mode	3: Value = 2.35389E-05 Freq = 7.72170E-04 (cycles/time)
4	Mode	4: Value = 8.23442E-05 Freq = 1.44423E-03 (cycles/time)
5	Mode	5: Value = 1.06414E-04 Freq = 1.64180E-03 (cycles/time)
6	Mode	6: Value = 1.37533E-04 Freq = 1.86648E-03 (cycles/time)
7	Mode	7: Value = 1.95172E-04 Freq = 2.22345E-03 (cycles/time)
8	Mode	8: Value = 1.99191E+10 Freq = 22462. (cycles/time)
9	Mode	9: Value = 2.00894E+10 Freq = 22558. (cycles/time)
10	Mode	10: Value = 2.78257E+10 Freq = 26549. (cycles/time)

Figure 53: First 10 mode Natural frequencies(f_n) of the anisotropic cylindrical model

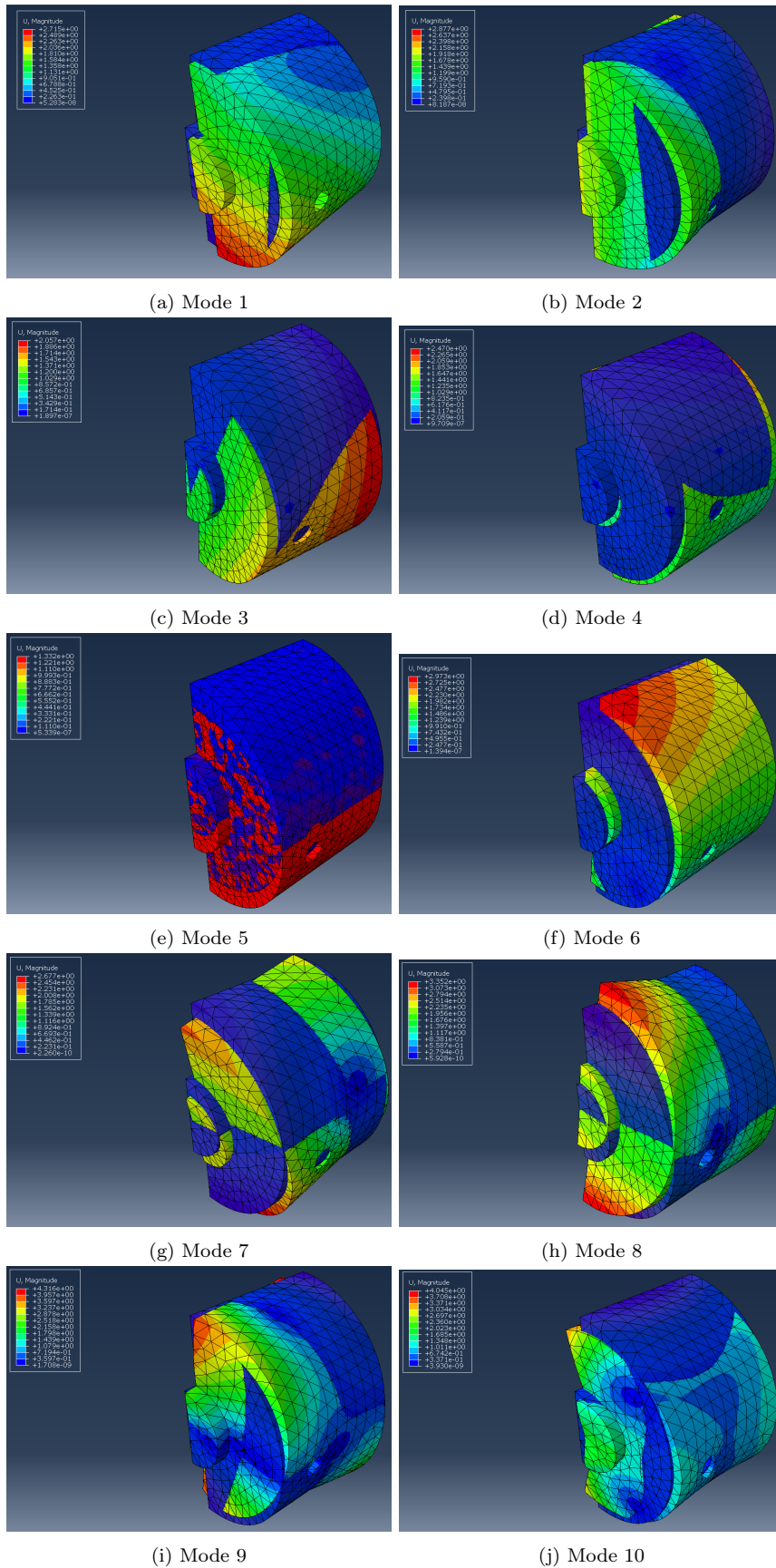


Figure 54: Initial 10 modes of frequencies of anisotropic cylindrical model

4.3.2 Modal analysis of rectangular model with isotropic material properties

The first ten natural frequencies of the rectangular model with isotropic material properties are depicted in Figure 55. Figure 56 depicts the displacement of these ten natural frequencies as mode shapes.

0	Increment	0: Base State
1	Mode	1: Value = -2.10331E-12 Freq = 0.0000 (cycles/time)
2	Mode	2: Value = 1.96277E-13 Freq = 7.05106E-08 (cycles/time)
3	Mode	3: Value = 8.82669E-13 Freq = 1.49527E-07 (cycles/time)
4	Mode	4: Value = 0.20997 Freq = 7.29280E-02 (cycles/time)
5	Mode	5: Value = 51.398 Freq = 1.1410 (cycles/time)
6	Mode	6: Value = 77.910 Freq = 1.4048 (cycles/time)
7	Mode	7: Value = 266.05 Freq = 2.5960 (cycles/time)
8	Mode	8: Value = 420.46 Freq = 3.2635 (cycles/time)
9	Mode	9: Value = 450.08 Freq = 3.3765 (cycles/time)
10	Mode	10: Value = 598.73 Freq = 3.8944 (cycles/time)

Figure 55: First 10 mode Natural frequencies(f_n) of the isotropic rectangular model

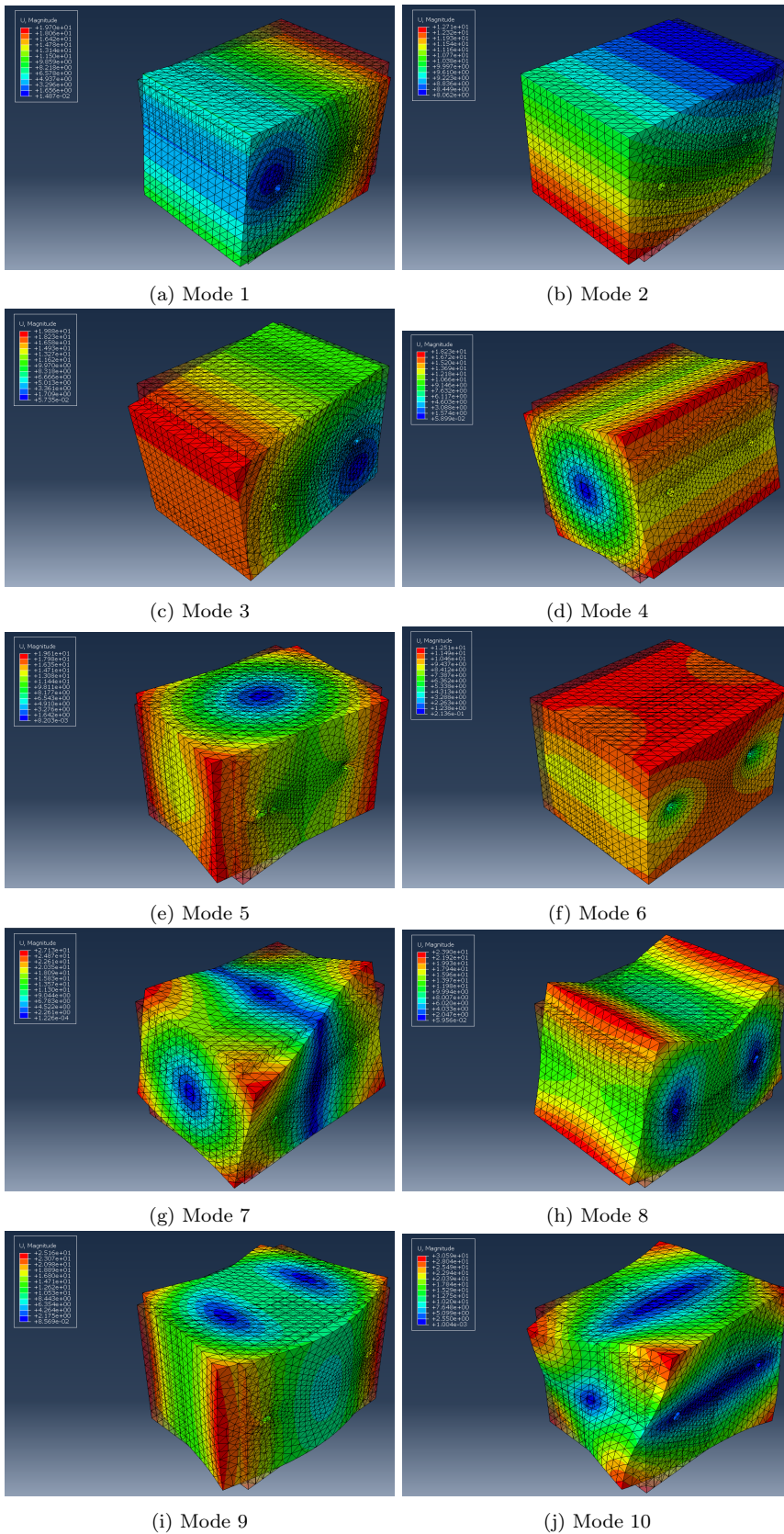


Figure 56: Initial 10 modes of frequencies of isotropic rectangular model

Rectangular model with anisotropic material properties with the stacking direction in element isoparametric direction Z-axis.

0	Increment	0: Base State
1	Mode	1: Value = -6.81509E-13 Freq = 0.0000 (cycles/time)
2	Mode	2: Value = 1.22691E-12 Freq = 1.76289E-07 (cycles/time)
3	Mode	3: Value = 2.06524E-12 Freq = 2.28720E-07 (cycles/time)
4	Mode	4: Value = 0.22130 Freq = 7.48710E-02 (cycles/time)
5	Mode	5: Value = 52.586 Freq = 1.1541 (cycles/time)
6	Mode	6: Value = 82.063 Freq = 1.4418 (cycles/time)
7	Mode	7: Value = 208.96 Freq = 2.3007 (cycles/time)
8	Mode	8: Value = 397.97 Freq = 3.1750 (cycles/time)
9	Mode	9: Value = 428.90 Freq = 3.2961 (cycles/time)
10	Mode	10: Value = 460.50 Freq = 3.4153 (cycles/time)

Figure 57: First 10 mode Natural frequencies(f_n) of the isotropic rectangular model

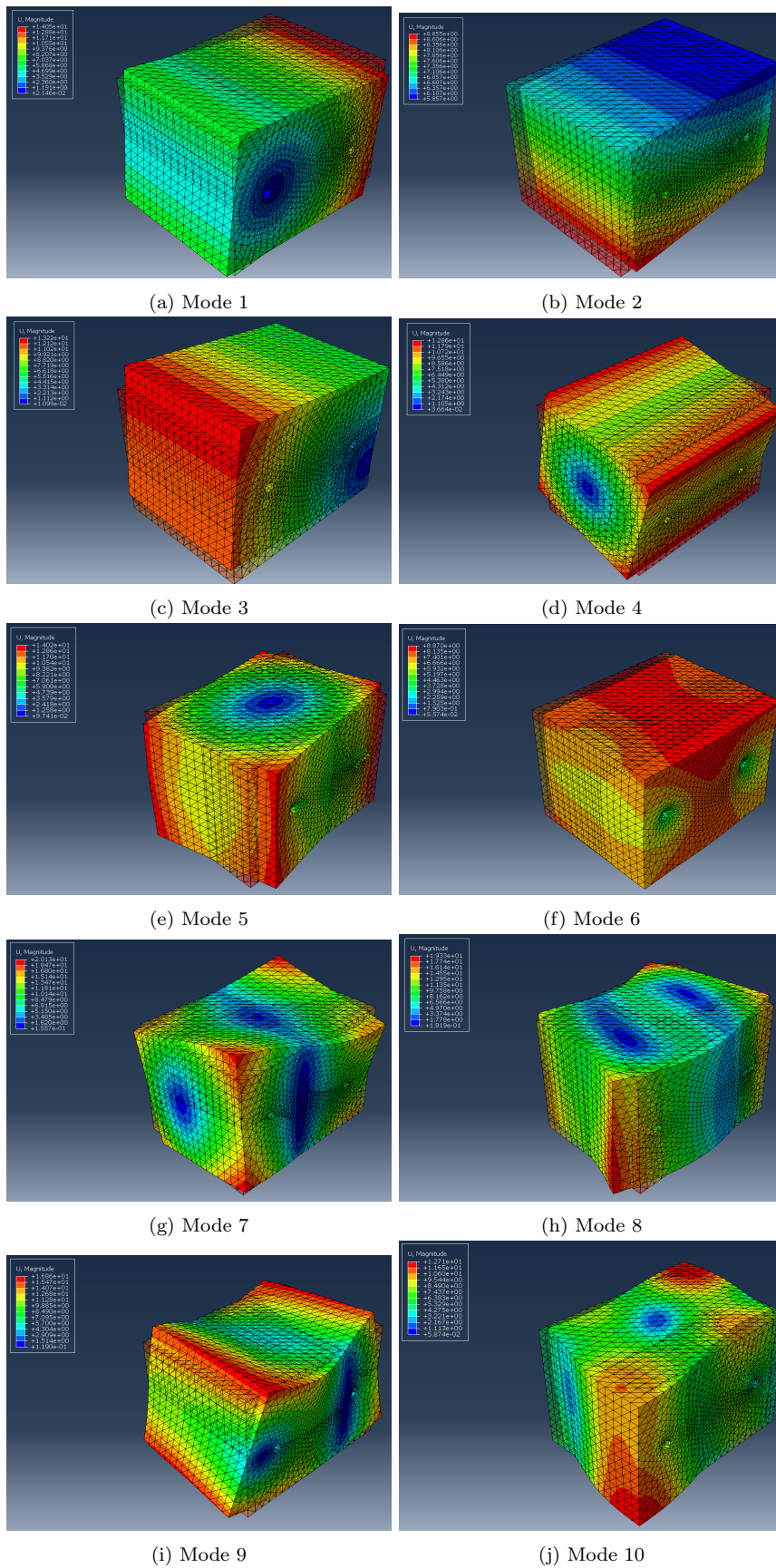


Figure 58: Initial 10 modes of frequencies of isotropic rectangular model

Rectangular model with anisotropic material properties with the stacking direction in element isoparametric direction Z-axis which is from bottom to top and additional rotation of 90 degrees with respect to Y-axis of orientation is considered.

0	Increment	0: Base State
1	Mode	1: Value = 2.84669E-13 Freq = 8.49161E-08 (cycles/time)
2	Mode	2: Value = 8.83603E-13 Freq = 1.49606E-07 (cycles/time)
3	Mode	3: Value = 3.91524E-12 Freq = 3.14919E-07 (cycles/time)
4	Mode	4: Value = 0.20411 Freq = 7.19046E-02 (cycles/time)
5	Mode	5: Value = 48.983 Freq = 1.1139 (cycles/time)
6	Mode	6: Value = 75.714 Freq = 1.3849 (cycles/time)
7	Mode	7: Value = 215.98 Freq = 2.3390 (cycles/time)
8	Mode	8: Value = 439.33 Freq = 3.3359 (cycles/time)
9	Mode	9: Value = 465.45 Freq = 3.4336 (cycles/time)
10	Mode	10: Value = 499.76 Freq = 3.5580 (cycles/time)

Figure 59: First 10 mode Natural frequencies(f_n) of the isotropic rectangular model

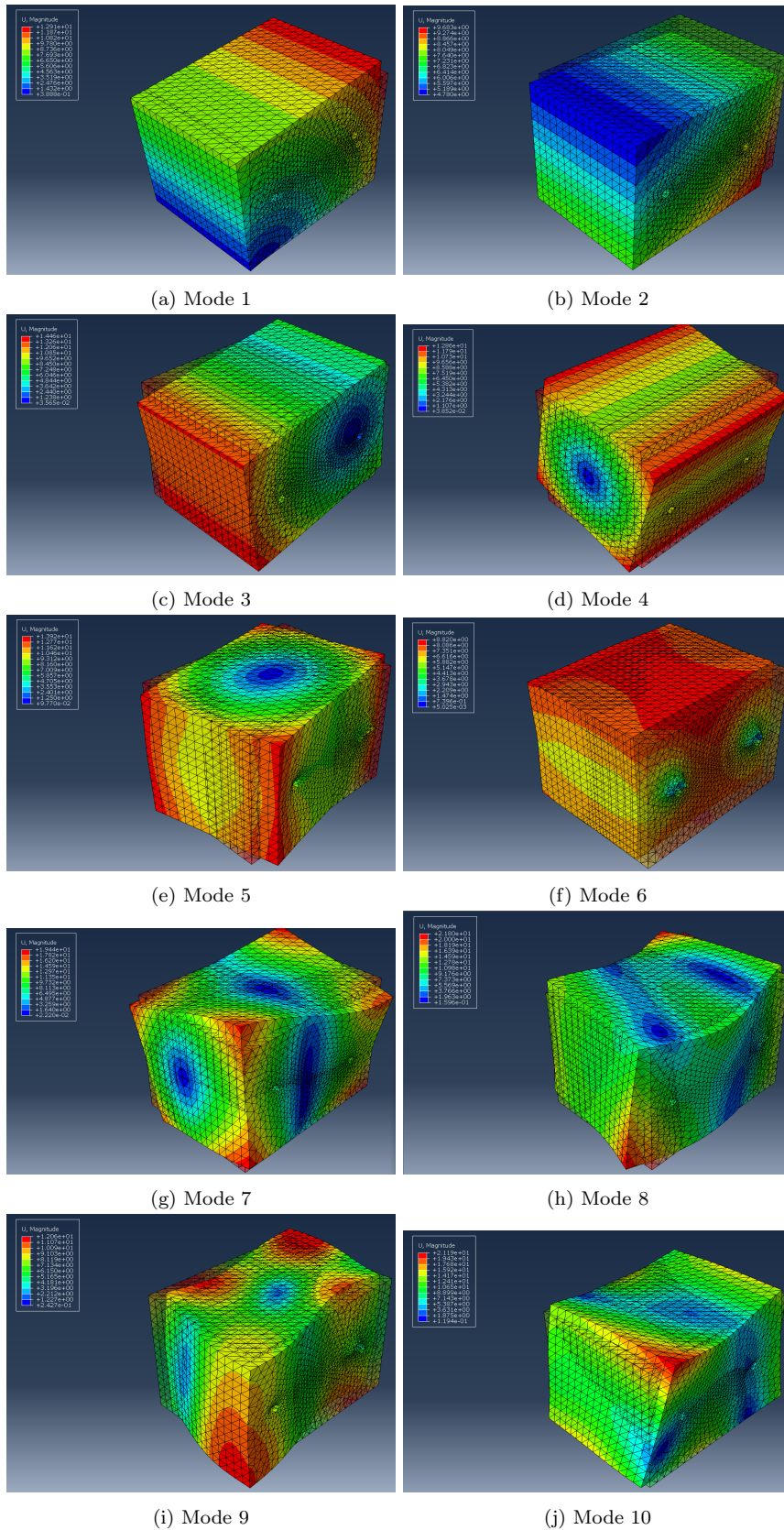


Figure 60: Initial 10 modes of frequencies of isotropic rectangular model

Rectangular model with anisotropic material properties with the stacking direction in element isoparametric direction Z-axis which is from bottom to top and additional rotation of 270 degrees with respect to Y-axis of orientation is considered.

0	Increment	0: Base State
1	Mode	1: Value = -4.53165E-13 Freq = 0.0000 (cycles/time)
2	Mode	2: Value = 2.87578E-13 Freq = 8.53489E-08 (cycles/time)
3	Mode	3: Value = 2.92644E-12 Freq = 2.72264E-07 (cycles/time)
4	Mode	4: Value = 0.20406 Freq = 7.18947E-02 (cycles/time)
5	Mode	5: Value = 48.981 Freq = 1.1139 (cycles/time)
6	Mode	6: Value = 75.711 Freq = 1.3848 (cycles/time)
7	Mode	7: Value = 215.98 Freq = 2.3390 (cycles/time)
8	Mode	8: Value = 439.32 Freq = 3.3359 (cycles/time)
9	Mode	9: Value = 465.44 Freq = 3.4336 (cycles/time)
10	Mode	10: Value = 499.78 Freq = 3.5580 (cycles/time)

Figure 61: First 10 mode Natural frequencies(f_n) of the isotropic rectangular model

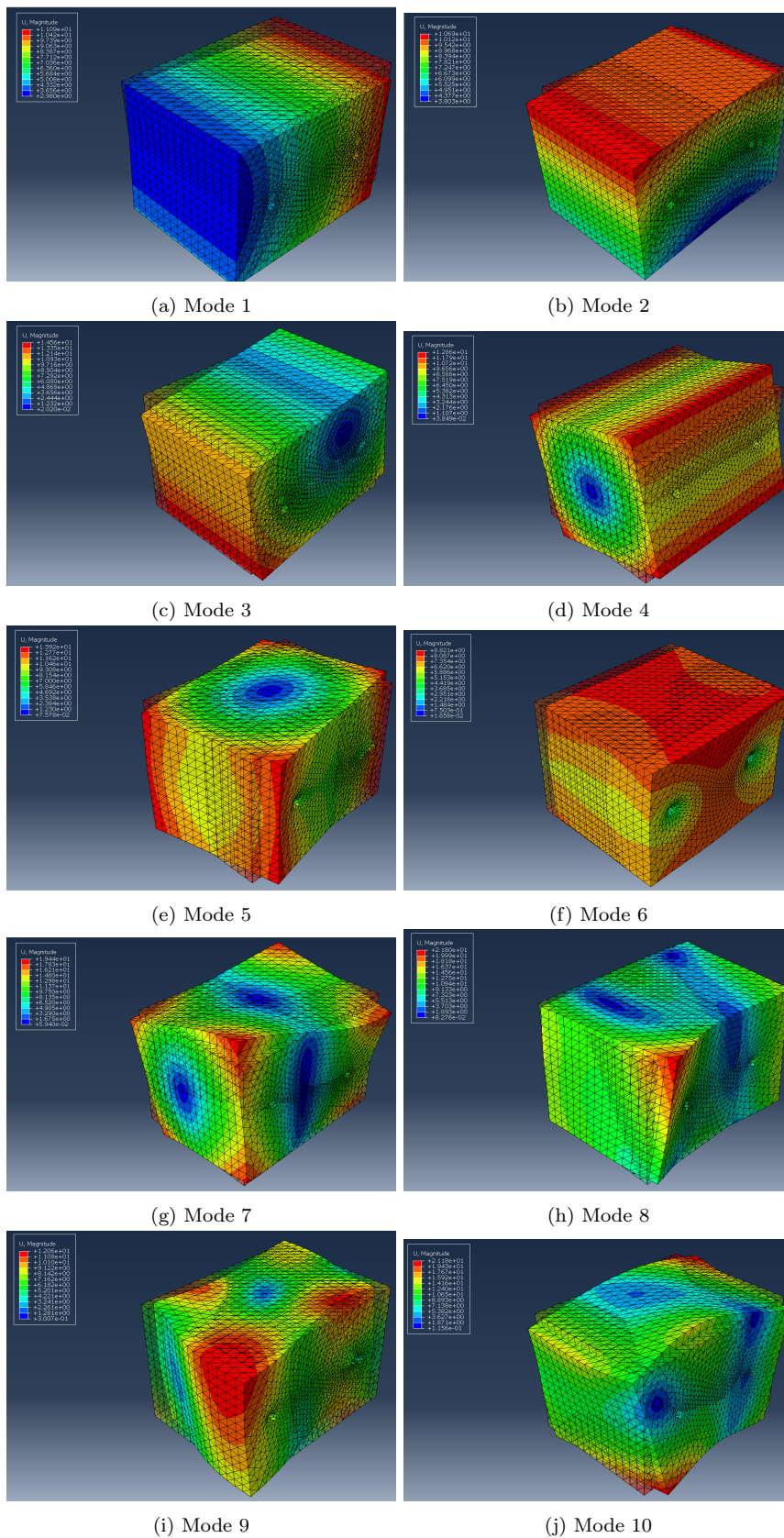


Figure 62: Initial 10 modes of frequencies of isotropic rectangular model

The figure 63 shows the comparison chart of frequencies for different cylindrical models used. By comparison, it is evident that the trend for all anisotropic cylindrical models are similar. Whereas, the isotropic model behaves differently with a higher trend, comparatively. In anisotropic models, the first 7 modes suggests almost 0 frequency. Although, we can see a sudden spike of frequency from mode 7 to mode 8. Whereas, in isotropic model, we notice a gradual increase in frequency right from 1st mode to the 10th mode.

The figure 64 shows the comparison chart of frequencies for rectangular models. From the results obtained, it is evident that all the rectangular model behaves almost identically. The trendline suggests that for all the rectangular models have similar frequencies right from mode 1 to mode 10.

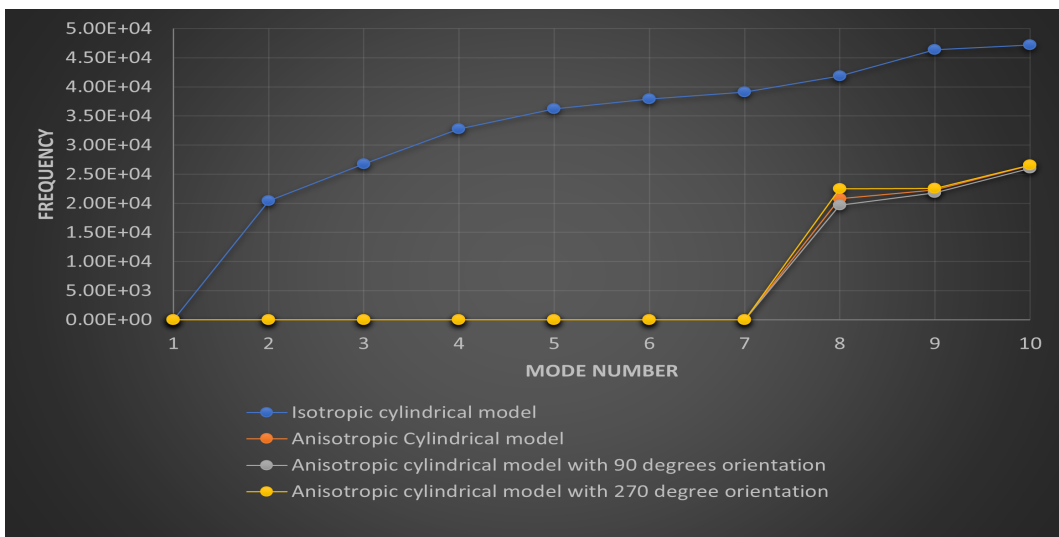


Figure 63: Mode number vs frequency for cylindrical model

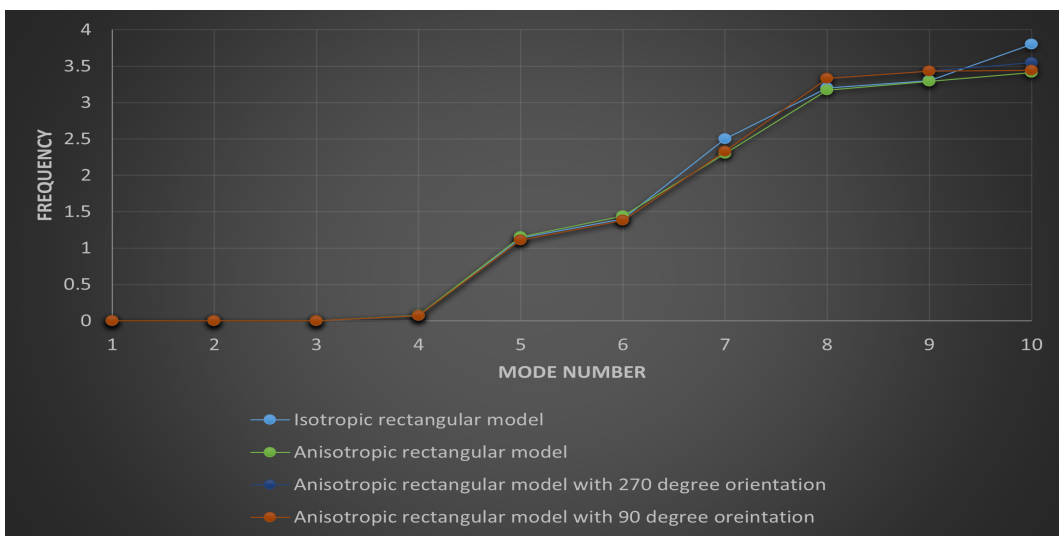


Figure 64: Mode number vs frequency for rectangular model

5 Discussion and Conclusions

In order to obtain accurate results, FE simulations take more time. All of the results mentioned in the results sections are apparent for comparison. The quarter half of cylindrical models were simulated and represent as half symmetric in result section and rectangular models are simulated and represent in complete models. Because a single simulation took around 30 to 60 hours to complete, all of the results of the simulations are considered and studied qualitatively, at the expense of quantitative analysis. That is why all models are based on 0.1m/s^2 force. Figure 16 depicts the z-direction deformation for a 0.1 m/s^2 acceleration in the positive Y-direction for an isotropic material model. These results, which are nearly 90 to 95 percent close to the reference paper, were obtained after several simulations with different loads and boundary conditions. The outcomes are considered in two directions, X and Z. To investigate the deformation and stress distribution behavior of anisotropic materials and compare them to isotropic materials, additional simulations were performed by changing the anisotropic orientation while keeping all loads and boundary conditions constant. Figures 14 and 18 show that the deformation patterns are similar in the x-direction, and the anisotropic model deformed more than the isotropic model under the same load conditions. When we look at the results in Z-direction from Figures 16 and 20, we can see that deformation is slightly more significant in the isotropic model than in the anisotropic model due to the orientation's direction. When it comes to stress distribution, as shown in figures 17 and 18 for the isotropic model and figure 21 and figure 22 for the anisotropic model, both principal and Von Mises stresses are more significant in the anisotropic material model and are concentrated near the circumference of the circular mirror where the load is applied. In contrast, fewer stresses are induced near the support points.

For a better understanding of anisotropic material behavior, simulations were conducted by rotating the local coordinate system concerning the global coordinate system. Due to time constraints, only three material orientations (0,90,270 degrees) were simulated. It can be seen that the deformation in the X-direction of an anisotropic material model for different material orientations has the same deformation pattern. Still, the model with no altered material orientation has deformed more than the other two orientations. Figures 20, figure 24, and figure 28 show the deformation in the Z-direction. The patterns remained the same, but the model with the unaltered material orientation had more deformation. From the figure 21, figure 22, figure 25, figure 26, figure 29, and figure 30, Both stresses are increased in the model with unaltered material orientation, and stresses are induced in the same area as in the isotropic material model. We can also see that the anisotropic model has minor deformation and stresses than the isotropic model because it has an additional material orientation rotation of 90 and 270 degrees.

A rectangular CAD model with the same material properties, load, and boundary conditions was created to gain a better understanding of the material behavior. Figure 16 and figure 32 show that the deformation pattern for the cylindrical and rectangular models is not the same and that the rectangular model is more deformed,

maybe because of the geometrical differences. Comparing isotropic and anisotropic rectangular models is made in the same way that the comparison of cylindrical models is made. When comparing the rectangular isotropic and anisotropic models in figure 31 and figure 35, it is clear that the deformation pattern is not uniform and is distributed unevenly throughout the model in the X direction, with the anisotropic model having deformed more than the isotropic model. When the results from figure 32 and figure 36 are viewed in the Z direction, the distortion pattern is the same, and anisotropic material has slightly more deformation value. The maximum Von Mises stress for the anisotropic model is more than double that of the isotropic model, and also the stress distribution patterns are not the same, but the minimum Von Mises stress value is similar, as shown in figures 33 and figure 37. Figures 34 and figure 38 show the maximum principal stress. The maximum and minimum values of the anisotropic model are more than double those of the isotropic model. Figure 35, figure 39, and figure 43 show the results of anisotropic models. The original material orientation model deforms more in the X-direction than the 90 and 270-degree material orientation models. The deformation results in the Z-direction are the same as the X-direction in figure 36, figure 40, and figure 44. When the stresses from figure 37, figure 41, figure 45 for Von-Mises stress and figure 38, figure 42, and figure 46 for maximum principal stress are studied, both Von Mises and maximum principal stress values are more than double in the model with original material orientation than in the model with 90 and 270-degree material orientation. The anisotropic model with the original material orientation has more deformation than the isotropic model in the rectangular model. However, anisotropic models with 90 and 270-degree material orientation deform less than isotropic models.

Modal analysis is used to find the eigenfrequencies, also known as natural frequencies, for all cylindrical and rectangular models. These frequencies are responsible for workpiece resonance, deformation, and failure. Modal analysis was used to simulate the first ten natural frequencies and mode shapes for all models. This will aid in determining the ideal frequencies required for the machining process of the workpiece due to the influence of vibration.

From the results obtained in section 4.3 for modal analysis, it is probable to conclude that the change in shape for each mode is varying completely for different cylindrical models. Whereas, for rectangular model, we see a similar behavior for some of the models. Figure 63 clearly indicates that the range of frequencies for anisotropic cylindrical models are almost identical for first 7 modes for cylindrical model. From mode 8 we see a sudden increase in frequency with a increase in magnitude of almost 20000 cycles/time. Whereas, for isotropic cylindrical model, we see a gradual increase in frequencies, ranging from 20000 to almost 50000 cycles/time. From figure 64, we can identify the range of frequencies for rectangular models for both isotropic and anisotropic models. Compared to cylindrical models, rectangular models have a similar trend of frequencies for all the isotropic and anisotropic models. From the comparison chart, we can identify the range of frequencies for first 4 modes to be almost 0, but we can identify increase in frequency from mode 5 with a magnitude of 1 cyle/time. But towards the end of the modal analysis, we can identify a gradual increase in frequencies with a magnitude of 3.5 to 4 cycles/time. This difference in

frequencies for rectangular and cylindrical models maybe because of the geometrical differences and changes in material properties.

With all of the comparisons and observations made between isotropic and anisotropic material orientation models, we can conclude that it is critical to study the material properties and its behavior under loading conditions in order to find the ideal working condition. Especially when anisotropic materials are taken into account, as they exhibit different material properties in different directions. Different anisotropic material orientations cause varying degrees of deformation and stress. By knowing the material behavior before machining, it is possible to reduce the deformation, induced stresses, and vibrations of models during machining by supporting the model in a specific position. It is also critical to investigate the material's behavior concerning the geometry of the model being used. We can achieve a nearly vibration-insensitive model by simulating and studying different orientations of the material layups in the anisotropic model.

References

- [1] Nazarova T, Riehle F, Sterr U. Vibration-insensitive reference cavity for an ultra-narrow-linewidth laser. *Applied Physics B*. 2006;83(4):531–536.
- [2] Fu ZF, He J. *Modal analysis*. Elsevier; 2001.
- [3] Reda H, Karathanasopoulos N, Elnady K, Ganghoffer JF, Lakiss H. The role of anisotropy on the static and wave propagation characteristics of two-dimensional architected materials under finite strains. *Materials and Design*. 2018;147:134–145. Available from: <https://doi.org/10.1016/j.matdes.2018.03.039>.
- [4] Shih R. *Introduction to finite element analysis using solidworks simulation 2014*. SDC publications; 2014.
- [5] Millo J, Magalhães D, Mandache C, Le Coq Y, English E, Westergaard P, et al. Ultrastable lasers based on vibration insensitive cavities. *Physical Review A*. 2009;79(5):053829.
- [6] Quessada A, Kovacich RP, Courtillot I, Clairon A, Santarelli G, Lemonde P. The Dick effect for an optical frequency standard. *Journal of Optics B: Quantum and Semiclassical Optics*. 2003;5(2):S150.
- [7] Ludlow AD, Zelevinsky T, Campbell G, Blatt S, Boyd M, de Miranda MH, et al. Sr lattice clock at 1×10^{-16} fractional uncertainty by remote optical evaluation with a Ca clock. *Science*. 2008;319(5871):1805–1808.
- [8] Coppola G. Stabilization of a diode laser onto a stable high-finesse cavity for coherent manipulation of Sr + ions. 2000.
- [9] Hall J, Taubman M, Ye J. *Laser Stabilization*. 1999 jan.
- [10] Prevost E, Thomas L, Goff RL, Bize S, Santarelli G, Prevost E, et al. Prototype of an ultra-stable optic cavity for space applications To cite this version : Prototype of an ultra-stable optical cavity for space applications . 2013.
- [11] Suslick KS. *Encyclopedia of physical science and technology*. Sonoluminescence and sonochemistry, 3rd edn Elsevier Science Ltd, Massachusetts. 2001:1–20.
- [12] Ravindra D, Ghantasala MK, Patten J. Ductile mode material removal and high-pressure phase transformation in silicon during micro-laser assisted machining. *Precision Engineering*. 2012;36(2):364–367. Available from: <https://www.sciencedirect.com/science/article/pii/S0141635912000025>.
- [13] Debroy A, Chakraborty S. Non-conventional optimization techniques in optimizing non-traditional machining processes: A review. *Management science letters*. 2013;4(1):23–38.
- [14] Šajgalík M, Kušnerová M, Harničárová M, Valíček J, Czán A, Czánová T, et al. Analysis and prediction of the machining force depending on the parameters of trochoidal milling of hardened steel. *Applied Sciences (Switzerland)*. 2020;10(5):1–19.

- [15] Shreyas RR, Sachin BSKK, Nanjundeswaraswamy TS. Selection of Non-Traditional Machining Process. *International Journal of Engineering Research and Technology (IJERT)*. 2019;8(11):148–155. Available from: <https://www.ijert.org>.
- [16] Kosky P, Balmer RT, Keat WD, Wise G. *Exploring engineering: an introduction to engineering and design*. Academic Press; 2015.
- [17] Jurčius A, Valiulis A, Kumšlytis V. Vibratory stress relieving - It's advantages as an alternative to thermal treatment. *Journal of Vibroengineering*. 2008 jan;10:123–127.
- [18] Nurhaniza M, Ariffin MKAM, Mustapha F, Baharudin BTHT. Analyzing the Effect of Machining Parameters Setting to the Surface Roughness during End Milling of CFRP-Aluminium Composite Laminates. *International Journal of Manufacturing Engineering*. 2016;2016:1–9.
- [19] Gökçe H, Yeşilay R, Uçak N, Teke A, Çiçek A. Improvement of Machining Processes: A Case Study. *Academic Perspective Procedia*. 2019 nov;2:634–641.
- [20] Gandhi MV, Thompson BS. Automated design of modular fixtures for flexible manufacturing systems. *Journal of Manufacturing Systems*. 1986;5(4):243–252.
- [21] Kolluru K, Axinte D, Becker A. A solution for minimising vibrations in milling of thin walled casings by applying dampers to workpiece surface. *CIRP Annals - Manufacturing Technology*. 2013;62(1):415–418. Available from: <http://dx.doi.org/10.1016/j.cirp.2013.03.136>.
- [22] Pan CT, Hocheng H. Evaluation of anisotropic thermal conductivity for unidirectional FRP in laser machining. *Composites - Part A: Applied Science and Manufacturing*. 2001;32(11):1657–1667.
- [23] Al Ba'Ba'A H, Nouh M. An investigation of vibrational power flow in one-dimensional dissipative phononic structures. *Journal of Vibration and Acoustics, Transactions of the ASME*. 2017;139(2):1–10.
- [24] Beards CF, Miao M. *Structural Vibration: Analysis and Damping*. Elsevier. 1996:289.
- [25] Floden O. *Vibration transmission in lightweight buildings*. vol. 14; 2016.
- [26] Hansen C. *Foundations of Vibroacoustics*. CRC Press; 2018.
- [27] Fung Y. Elasticity of soft tissues in simple elongation. *American Journal of Physiology-Legacy Content*. 1967;213(6):1532–1544.
- [28] Wu Z, Zhang L, Liu W. Structural anisotropy effect on the nanoscratching of monocrystalline 6H-silicon carbide. *Wear*. 2021;(November 2020):203677. Available from: <https://doi.org/10.1016/j.wear.2021.203677>.
- [29] Horgan CO, Murphy JG, Saccomandi G. The complex mechanical response of anisotropic materials in simple experiments. *International Journal of Non-Linear Mechanics*. 2018;106(January):274–279. Available from: <https://doi.org/10.1016/j.ijnonlinmec.2018.05.025>.

- [30] Prall DM, Lakes R. Properties of a chiral honeycomb with a poisson's ratio of@ 1. *International Journal of Mechanical Sciences*. 1997;39:305–314.
- [31] Smith CW, Wootton RJ, Evans KE. Interpretation of experimental data for Poisson's ratio of highly nonlinear materials. *Experimental Mechanics*. 1999;39(4):356–362.
- [32] Wu Y, Yi N, Huang L, Zhang T, Fang S, Chang H, et al. Three-dimensionally bonded spongy graphene material with super compressive elasticity and near-zero Poisson's ratio. *Nature Communications*. 2015;6.
- [33] Xu S, Shen J, Zhou S, Huang X, Xie Y. Design of lattice structures with controlled anisotropy. *Materials & design*. 2016 jan;93:443–447.
- [34] Meza LR, Das S, Greer JR. Strong, lightweight, and recoverable three-dimensional ceramic nanolattices. *Science (New York, NY)*. 2014 sep;345(6202):1322–1326.
- [35] Hosokawa M. *Nanoparticle Technology Handbook*. Amsterdam: Elsevier; 2008. p. v–vi. Available from: <https://www.sciencedirect.com/science/article/pii/B9780444531223500015>.
- [36] Mirzai A, Ahadi A, Melin S, Olsson PAT. First-principle investigation of doping effects on mechanical and thermodynamic properties of Y₂SiO₅. *Mechanics of Materials*. 2021;154.
- [37] Sokolnikoff IS. *Mathematical theory of elasticity*; 1946. .
- [38] Mase GT, Smelser RE, Mase GE. *Linear Elasticity. Continuum Mechanics for Engineers*. 2020:239–298.
- [39] Avitabile P. Experimental modal analysis. *Sound and vibration*. 2001;35(1):20–31.
- [40] Edskär I. *Modal Analysis, Dynamic Properties and Horizontal Stabilisation of Timber Buildings*; 2018. Available from: www.ltu.se.
- [41] Schwarz BJ, Richardson MH. Método de análisis modal experimental. 1999:1–12. Available from: <http://papers.vibetech.com/Paper28-ExperimentalModalAnalysis.pdf>.
- [42] Shin C, Ho Cha Y. Waveform inversion in the Laplace—Fourier domain. *Geophysical Journal International*. 2009 jun;177(3):1067–1079. Available from: <https://doi.org/10.1111/j.1365-246X.2009.04102.x>.
- [43] Ha NS, Vang HM, Goo NS. Modal Analysis Using Digital Image Correlation Technique: An Application to Artificial Wing Mimicking Beetle's Hind Wing. *Experimental Mechanics*. 2015;55(5):989–998.
- [44] Guillaume P. *Modal analysis*. Department of Mechanical Engineering, Vrije Universiteit Brussel, Pleinlaan. 2007;2:4–6.

- [45] Ha N, Vang H, Goo N. Modal analysis using digital image correlation technique: an application to artificial wing mimicking beetle's hind wing. *Experimental Mechanics*. 2015;55(5):989–998.
- [46] Doebling SW, Farrar CR, Prime MB. A summary review of vibration-based damage identification methods. *Shock and Vibration Digest*. 1998;30(2):91–105.
- [47] Siller E, Ramon H. *Non-linear modal analysis methods for engineering structures*; 2004. .
- [48] Heylen W, Lammens S, Sas P. *Modal Analysis Theory and Testing*. 1997:340. Available from: <https://pdfs.semanticscholar.org/bad9/0f4967dc926830c47226f2157ce4727a3983.pdf>.
- [49] Maia NMM, Silva JMM. Modal analysis identification techniques. *Philosophical Transactions of the Royal Society A: Mathematical, Physical and Engineering Sciences*. 2001;359(1778):29–40.
- [50] Jihong Choi, Sangkee Min, David A Dornfeld A , Mahboob Alam, Tzong T.J. Modeling of interlayer gap formation in drilling of a multi-layered material. 6th CIRP International Workshop on Modeling of Machining Operations. 2003:113–118.
- [51] Wang GD, Melly SK. Three-dimensional finite element modeling of drilling CFRP composites using Abaqus/CAE: a review. *International Journal of Advanced Manufacturing Technology*. 2018;94(1-4):599–614.
- [52] Khennane A. *Introduction to finite element analysis using MATLAB® and abaqus*. CRC Press; 2013.
- [53] Vijayaraghavan A, Gardner JD, Dornfeld DA. Comparative study of finite element simulation software. Consortium on Deburring and Edge Finishing. 2005.

references